Space Launch System Liftoff and Transition Aerodynamic Characterization in the NASA Langley 14- by 22-Foot Subsonic Wind Tunnel

Jeremy T. Pinier[1]*, Gary E. Erickson[1]†, John W. Paulson[3]‡,
William G. Tomek[1]*, David W. Bennett[1]§, and John A. Blevins[2]¶

[1]*NASA Langley Research Center, Hampton, VA, 23681*

[2]*NASA Marshall Space Flight Center, Huntsville, AL, 35811*

[3]*Analytical Mechanics Associates Inc., Hampton, VA, 23666*

Notice to the Reader

The Space Launch System, including its predicted performance and certain other features and characteristics, has been defined by the U.S. Government to be Sensitive But Unclassified (SBU). Information deemed to be SBU requires special protection and may not be disclosed to an international audience, such as the audience that might be present at the 2015 AIAA SciTech Conference. To comply with SBU restrictions, details such as absolute values have been removed from some plots and figures in this paper. It is the opinion of the authors that despite these alterations, there is no loss of meaningful technical content. Analytical methodologies and experimental capabilities are discussed; significant technical results are presented; and meaningful conclusions and lessons learned are provided.

A 1.75% scale force and moment model of the Space Launch System was tested in the NASA Langley Research Center 14- by 22-Foot Subsonic Wind Tunnel to quantify the aerodynamic forces that will be experienced by the launch vehicle during its liftoff and transition to ascent flight. The test consisted of two parts: the first was dedicated to measuring forces and moments for the entire range of angles of attack (0° to 90°) and roll angles (0° to 360°). The second was designed to measure the aerodynamic effects of the liftoff tower on the launch vehicle for ground winds from all azimuthal directions (0° to 360°), and vehicle liftoff height ratios from 0 to 0.94. This wind tunnel model also included a set of 154 surface static pressure ports. Details on the experimental setup, and results from both parts of testing are presented, along with a description of how the wind tunnel data was analyzed and post-processed in order to develop an aerodynamic database. Finally, lessons learned from experiencing significant dynamics in the mid-range angles of attack due to steady asymmetric vortex shedding are presented.

*Research Aerospace Engineer, Configuration Aerodynamics Branch, MS 499, Senior Member AIAA.

†Research Aerospace Engineer, Configuration Aerodynamics Branch, MS 499.

‡Research Aerospace Engineer, 21 Enterprise Parkway Suite 300, Associate Fellow AIAA

§Research Aerospace Engineer, Vehicle Analysis Branch, MS 451

¶Aerodynamics Team Lead, Aerosciences Branch, Senior Member AIAA.

Nomenclature

α	=	angle of attack, body axis system, deg
β	=	angle of sideslip, body axis system, deg
α_V	=	angle of attack, vertical-plane axis system, ALPHAV, deg
ϕ_V	=	roll angle, vertical-plane axis system, PHIV, deg
CAF	=	axial force coefficient, forebody
$CLLF$	=	rolling moment coefficient, forebody, reference at the balance moment center
$CLMF$	=	pitching moment coefficient, forebody, reference at the balance moment center
$CLNF$	=	yawing moment coefficient, forebody, reference at the balance moment center
CNF	=	normal force coefficient, forebody
CYF	=	side force coefficient, forebody
h	=	elevation of the base of the solid rocket booster (SRB) skirts from the mobile launched platform, $in.$
L	=	total height of the tower from the mobile launchpad platform, $in.$
Q	=	freestream dynamic pressure, lbf/ft^2
ϕ	=	vehicle roll angle, degrees
ψ	=	wind azimuth angle, degrees
V	=	freestream velocity, ft/s
Re	=	freestream unit Reynolds number

Introduction

The Space Launch System (SLS) is NASA's future cargo and crew launch vehicle that is being designed for beyond low Earth orbit (LEO) missions. Its core stage is a modified Space Shuttle external tank fitted with four RS-25 liquid rocket engines as the main propulsion system. Two five-segment solid rocket boosters (SRB) provide additional thrust for the first two minutes of flight. The crew-carrying versions of SLS are designed to carry the Orion Multi-Purpose Crew Vehicle (MPCV) with the launch abort system (LAS). NASA is currently designing a family of configurations of the SLS to accommodate crew and/or cargo of various sizes ranging in capabilities from the baseline 70-metric-ton payload to low Earth orbit for the Block 1 version named SLS-10000, to a 130-metric-ton payload to LEO for the Block 2 cargo-only version, named SLS-21000. A number of intermediate configurations are currently in the early design phases, and will provide a suite of capabilities that include cargo payloads of various sizes and the possibility of crew transportation along with the cargo. For each configuration, a significant amount of wind tunnel testing and computational fluid dynamics (CFD) is either planned or has already been completed. This analysis is being conducted to cover all phases of atmospheric flight of the launch vehicle, including liftoff, ascent, booster separation, and service module panel jettison. The SLS Aerodynamics Task Team is responsible for characterizing these aerodynamic environments and covers multiple sub-disciplines, including static aerodynamics, aeroelasticity, aeroacoustics, acoustics, and venting analysis. An overview of the SLS aerodynamic work can be found in Blevins et al.[1] The primary source of data for developing the static aerodynamic databases for SLS is from wind tunnel testing of scaled launch vehicle models. SLS-10000 is the current highest priority baseline SLS configuration. It has now been tested throughout the entire Mach range to support the characterization of aerodynamic environments. The low-subsonic Mach range testing for liftoff (Mach $\leq$ 0.2) is the subject of this paper. The subsonic, transonic and supersonic testing for ascent conditions (from Mach = 0.3 to Mach = 5), where the vehicle encounters maximum dynamic pressures in flight, was reported by Pinier et al.[2] and by Pritchett et al.[3] The highly dynamic booster separation event that occurs around Mach = 4.25 has also been tested extensively during two different wind tunnel tests, one of which has just recently been completed at the NASA Langley Research Center (LaRC) Unitary Plan Wind Tunnel (UPWT) and will be reported in the near future.

To characterize the aerodynamics of the vehicle during liftoff, test data needs to be obtained in the incompressible or low-subsonic flow regime (Mach $\leq$ 0.2). This paper describes the 1.75% scale SLS wind tunnel test that was conducted at the NASA LaRC 14- by 22-Foot Subsonic Wind Tunnel (14x22 SWT) to develop the current version of the liftoff and transition aerodynamic database. This test builds on knowledge

and experience gained during testing of the liftoff aerodynamics of the Ares I launch vehicle in the same wind tunnel during the Constellation program. Capone et al.[4] describe this test in detail. Many valuable lessons were learned during the Ares I test, which enabled a successful and efficient SLS test. In parallel to the wind tunnel test, CFD simulations were conducted on the SLS liftoff configuration in order to gather information about distributed aerodynamic loading on the vehicle. Through CFD, a very high spatial resolution surface pressure mapping can be achieved and integrated to result in a set of lineloads, or distributed sectional loads. The liftoff phase of flight is, however, extremely challenging for CFD simulations because of the very low speed flow where viscous effects are strong and because of the high angles of attack experienced by the vehicle during liftoff ranging from -90° to 90° angle of attack. At these high attitudes, the flow is massively separated on the leeward side of the vehicle, and is highly unsteady, with strong vortex shedding in the wake of the vehicle. The CFD investigation is detailed in Krist et al.[5] To reduce the uncertainty in the CFD, a data fusion methodology based on a physics-based reduced-order model (PBROM) was developed by Carlson et al.[6] to combine the high-fidelity experimental data (surface pressures and integrated forces and moments) from the wind tunnel test with the simulation results. This resulted in a dataset of distributed aerodynamic quantities, calibrated by experimental data. Details on the acquisition of surface pressures in the wind tunnel test are presented in this paper.

I. Wind Tunnel Test Description

A. Wind Tunnel Facility

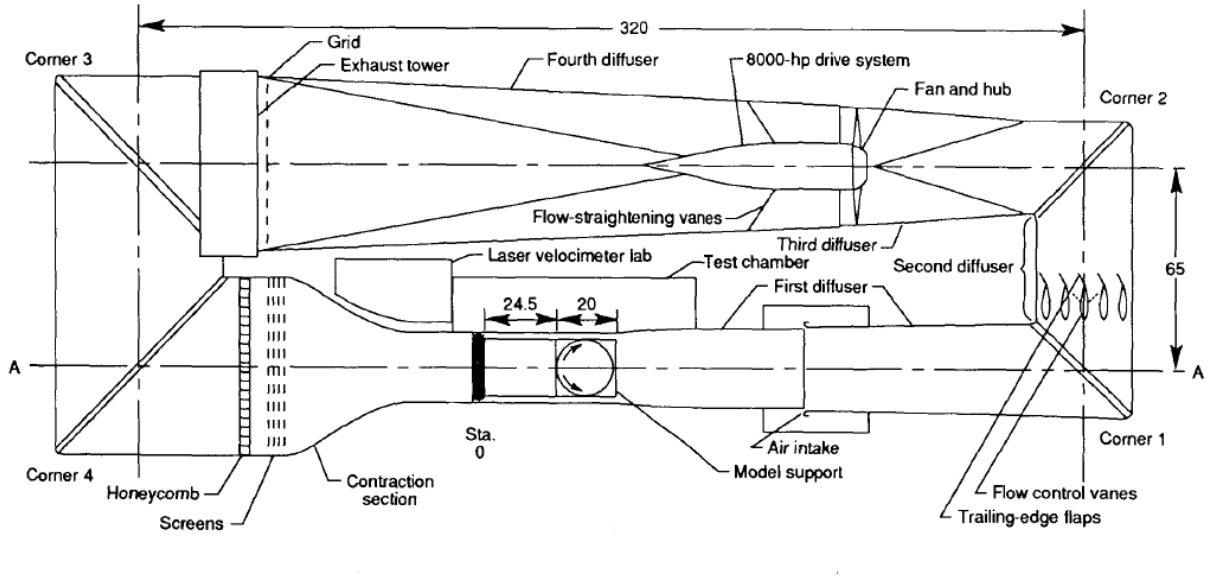

Figure 1. Schematic of the 14- by 22-Foot Subsonic Wind Tunnel main air circuit. Dimensions are given in feet.

The NASA LaRC 14x22 SWT is an atmospheric, low-speed wind tunnel with continuous control of Mach number from 0 to 0.3. Figure 1 shows a schematic of the recirculating wind tunnel.[7] The facility has a vertical post mounting system, as seen in Fig. 2, that was originally designed for ground effect testing of fighter and transport aircraft models. It has an angle of attack range of -10° to +50° if there are no offsets in place, and vertical motion range from the floor of the test section to about the test section centerline. The side walls and ceiling of the test section can be removed in order to minimize wall interference when testing large models or rotorcraft at low speeds. For the purpose of the experiment described in this paper, and because of the relatively small size and blockage ratio of the launch tower and SLS model, the side walls were closed, which resulted in better flow quality. The facility also is equipped with a boundary layer removal system that reduces the thickness of the boundary layer on the floor of the test section. The thickness of the boundary layer in the test section near the location of the model is about 8 inches. Because the wind tunnel model was always above this distance from the floor, it was decided not to remove the test section

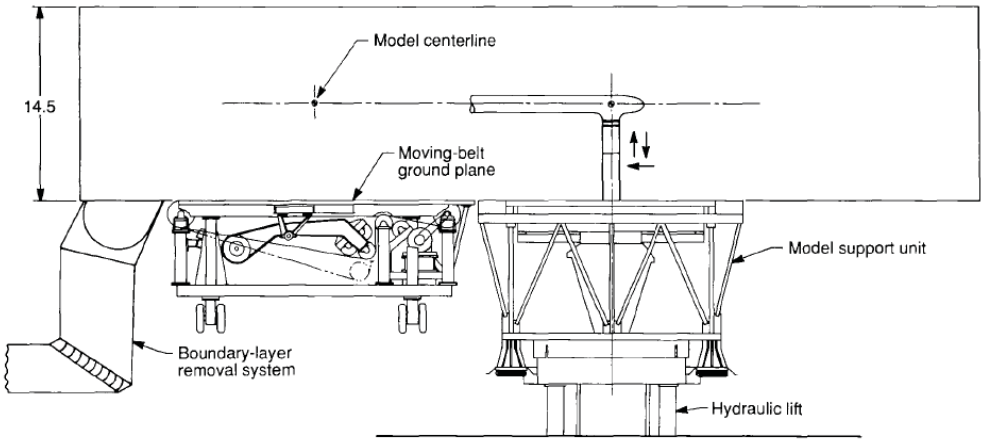

Figure 2. 14- by 22-Foot Wind Tunnel test section. Dimensions are given in feet.

boundary layer. Capone et al.[4] also recently showed during a very similar test conducted with the Ares I launch vehicle that the floor boundary layer effects were minimal and could be ignored.

B. Test Conditions

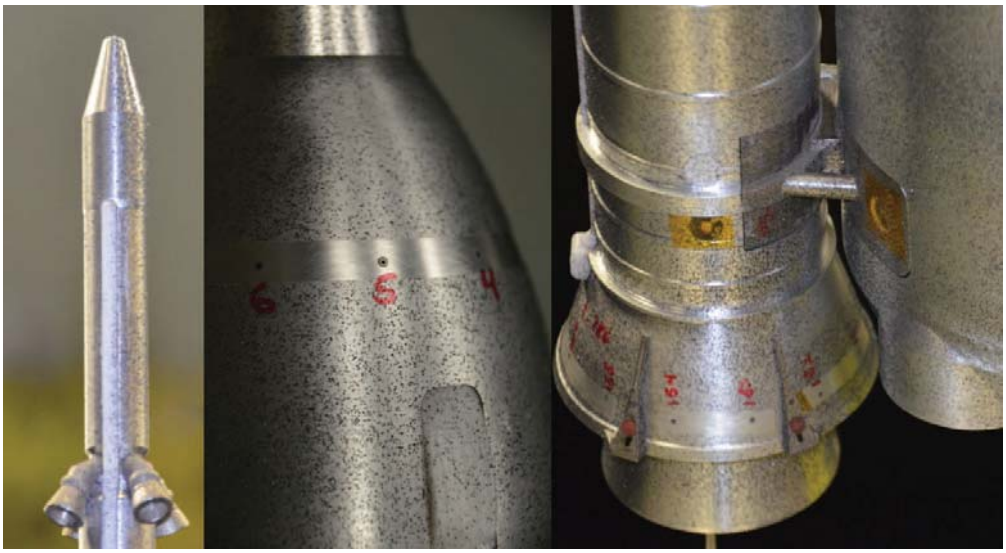

Figure 3. Close-up pictures of various surfaces on the SLS wind tunnel model showing the uniformly sprinkled #80-grit for boundary layer tripping.

Because of the scale of the model, the Reynolds number of the flow on the vehicle is lower than in full scale flight. It is therefore important to devise a strategy to trip the boundary layer to make it turbulent, like on the flight vehicle. Capone et al.[4] led a study of the most effective boundary layer tripping strategy on a slender launch vehicle that is pitched and rolled during testing. They found that a uniform sprinkling of #80-grit on the entire body was the most consistent and predictable way to trip the boundary layer. Given these results and the fact that the SLS vehicle is also a slender vehicle, the same strategy was implemented during this test. The pictures in Fig. 3 show close-ups of the model surface with #80-grit uniformly sprinkled and secured to the model with all-purpose spray adhesive. When applying the adhesive and grit, the surface pressure ports on the model were protected, as can be noted in the photos.

The wind tunnel is capable of running at dynamic pressures ranging from 10 to 120 lbf/ft^2, maximum air speeds of about 330 ft/s, and unit Reynolds numbers of close to 2×10^6 /ft. At the outset of the test, a

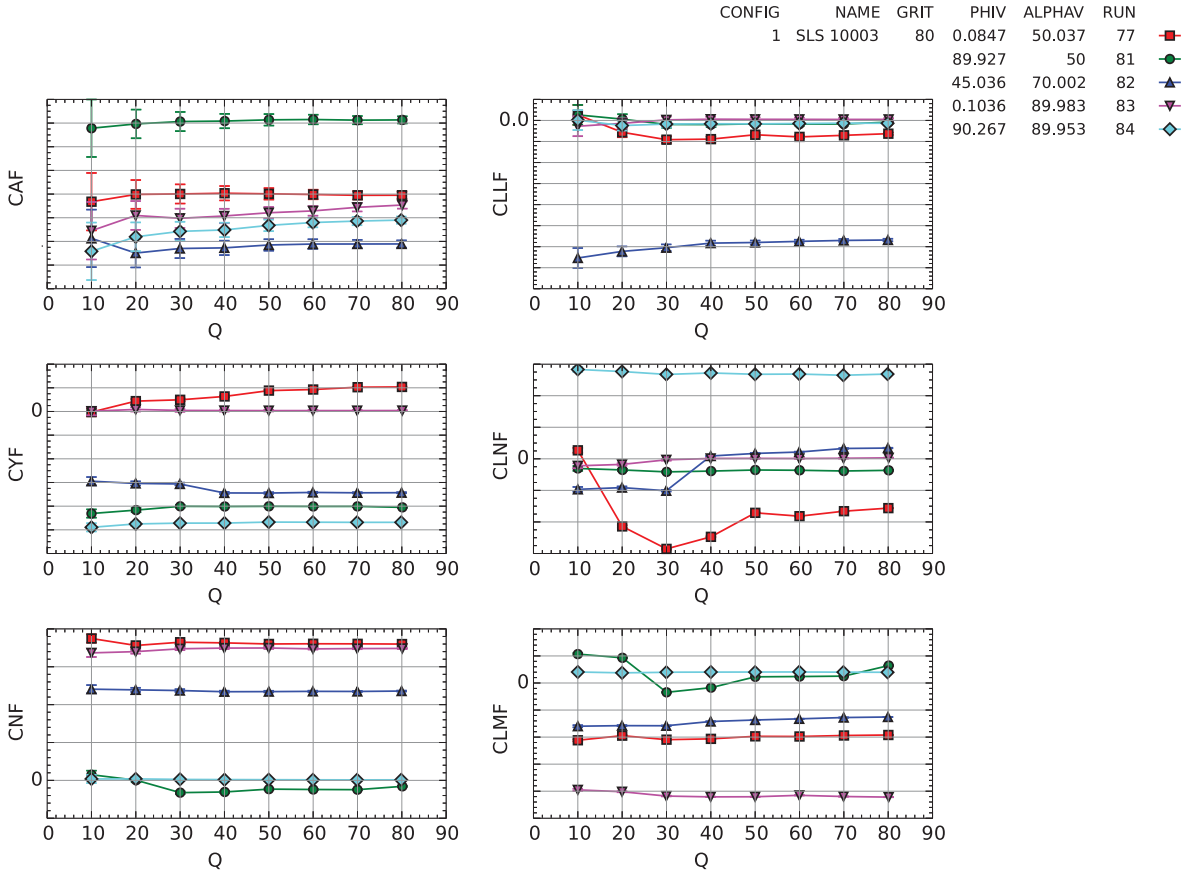

Figure 4. Aerodynamic coefficients for a series of 4 dynamic pressure sweeps from 10 to 80 lbf/ft^2.

series of dynamic pressure sweeps were performed to determine an appropriate dynamic pressure to run the entire test matrix. The model is mounted on a 6-component force-and-moment balance that is optimized for a particular loading range. At the very low dynamic pressures, the signal-to-noise ratio from the balance readings are too low. Additionally, there are boundary layer transition issues that make the data inconsistent from one run to another. This would result in poor repeatability and overall data quality. The balance is also limited in its maximum allowable loads. Based on this limitation, the maximum dynamic pressure allowed to safely run without exceeding load limits or model stress limits was 80 lbf/ft^2. Figure 4 shows how the six aerodynamic coefficients, even on the gritted configuration, have non-linear trends below a dynamic pressure of 40 lbf/ft^2, but converge to nearly constant values above. It was therefore decided to run the entire test matrix at a dynamic pressure of 50 lbf/ft^2, or 207 ft/s. The following table shows the wind tunnel flow conditions at the various dynamic pressures in the runs performed during this study with the main test condition used during the test in bold print.

Q (lbf/ft^2)	V (ft/s)	Mach	Re (/ft)
10	92	0.082	566,000
20	130	0.116	800,000
30	160	0.142	980,000
40	185	0.164	1,132,000
50	**207**	**0.183**	**1,267,000**
60	226	0.2	1,382,000
70	244	0.216	1,492,000
80	260	0.231	1,600,000

C. Model Description and Test Setup

To increase the long-term usefulness of the test data for the SLS program, a family of configurations was built and tested, including the highest priority SLS-10000 vehicle, otherwise known as Block I, that is currently manifested for its first test flight in 2017 or early 2018. Other configurations include longer versions of the SLS that are currently not slated to fly until the early 2020s. A detailed description of the four configurations tested is given in the following section.

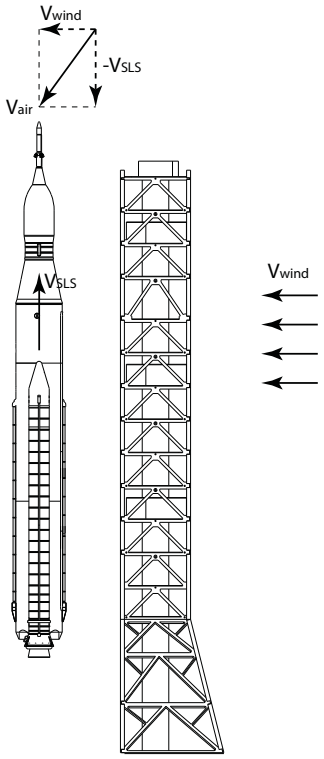

Figure 5. SLS at liftoff.

It is important to understand the limitations and assumptions that are made when conducting a simulation of a flight vehicle, whether in a wind tunnel or through CFD. Once these limitations are recognized, they can be evaluated to determine whether they will have an impact on the results. In the case of the liftoff phase of flight, for a given ground wind direction, the launch tower remains at a total angle of attack in the vicinity of 90°. As the vehicle lifts off the launch pad, it starts gaining longitudinal velocity, and the vehicle's total angle of attack decreases rapidly from 90° to under 10°. At any given time, the launch tower and the launch vehicle could therefore be at vastly different total angles of attack, even before the launch vehicle clears the tower. Figure 5 illustrates this with the example of a ground wind with a horizontal velocity of

V_{wind} and the SLS with a vertical velocity of V_{SLS}. The resultant freestream velocity vector V_{air} is therefore different from V_{wind}, as experienced by the launch tower.

In the wind tunnel (and in CFD), because it is a static simulation of the vehicle liftoff phase, the launch vehicle and the launch tower will always be at the same total angle of attack. The boundary conditions in an experiment or CFD simulation are global, i.e., the freestream incoming air for a wind tunnel experiment, or flow boundary conditions at the edges of the CFD domain determine the attitude of the tower and the launch vehicle at the same time. In order to capture the angle of attack effect for the vehicle while also measuring the tower interference aerodynamic effects, the wind tunnel test was designed in two parts. Results from both parts of the test are reported separately in this paper due to the vastly different experimental setup. The first part of testing, or "transition" testing, of the vehicle in free-air was conducted to capture the angle of attack, and angle of sideslip effects covering the entire range, from -90° to 90°. The second part of testing, or "tower effects" testing was conducted to measure the effects of the presence of the launch tower as a function of wind azimuth, with directions ranging from 0° to 355°, and vehicle liftoff ratio h/L, ranging from 0 to 1, where h is the vertical displacement of the vehicle, and L is the height of the tower. To build up the aerodynamic coefficient in a flight simulation, the baseline aerodynamic loads are based on the free-air transition testing added to an increment due to the tower effects that is based on the wind component V_{wind} of the velocity vector only. It is implicitly assumed that the tower effects do not depend on the actual vehicle angle of attack. This is not a bad assumption since, even though the vehicle might be at a low total angle of attack, it stays very close to being parallel to the tower.

The following sections describe the four scaled SLS configurations tested, and the test setup for both the transition testing and the tower effects testing.

1. SLS Configurations

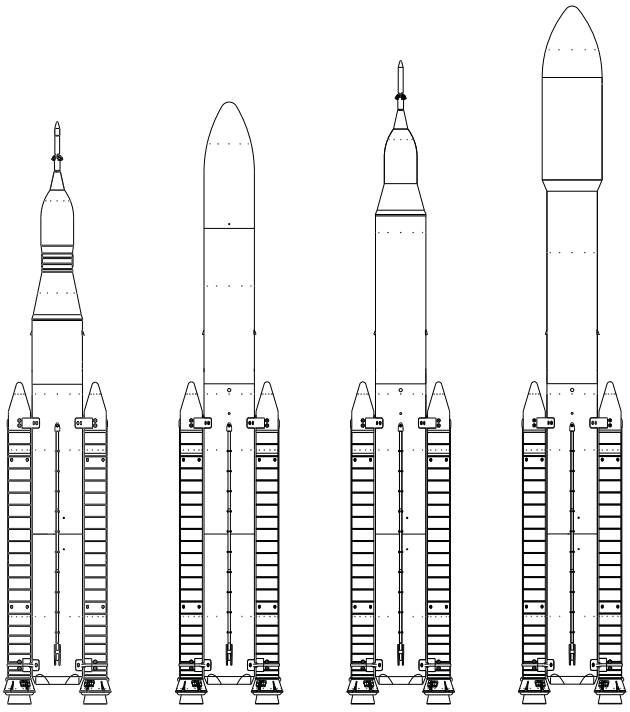

Figure 6. Schematic of the 4 wind tunnel models built and tested during Test 609. From left to right: SLS-10000, SLS-27000, SLS-28000, and SLS-21000.

Four different 1.75%-scale SLS configurations were tested during Test number 609 at the NASA LaRC 14- by 22-Foot wind tunnel: SLS-10000, SLS-27000, SLS-28000, and SLS-21000. Figure 6 shows these vehicle configurations from left to right in the same order. The wind tunnel models were designed to have a common core stage and solid rocket boosters (SRB), with the 6-component force and moment balance mounted in the lower core stage part, which allowed for model changes from one configuration to the next to be simple. Each

model was equipped with 154 surface pressure ports distributed around the circumference at six different cross-sections of the vehicle. These pressure ports are visible in the schematics of Fig. 6 as small dots. Each port was a 0.040-inch inner diameter hole connected to a pressure tube and an electronically scanned pressure module (ESP) for data acquisition. Both boosters and the core, were each equipped with a separate ESP module.

2. Transition Testing Setup

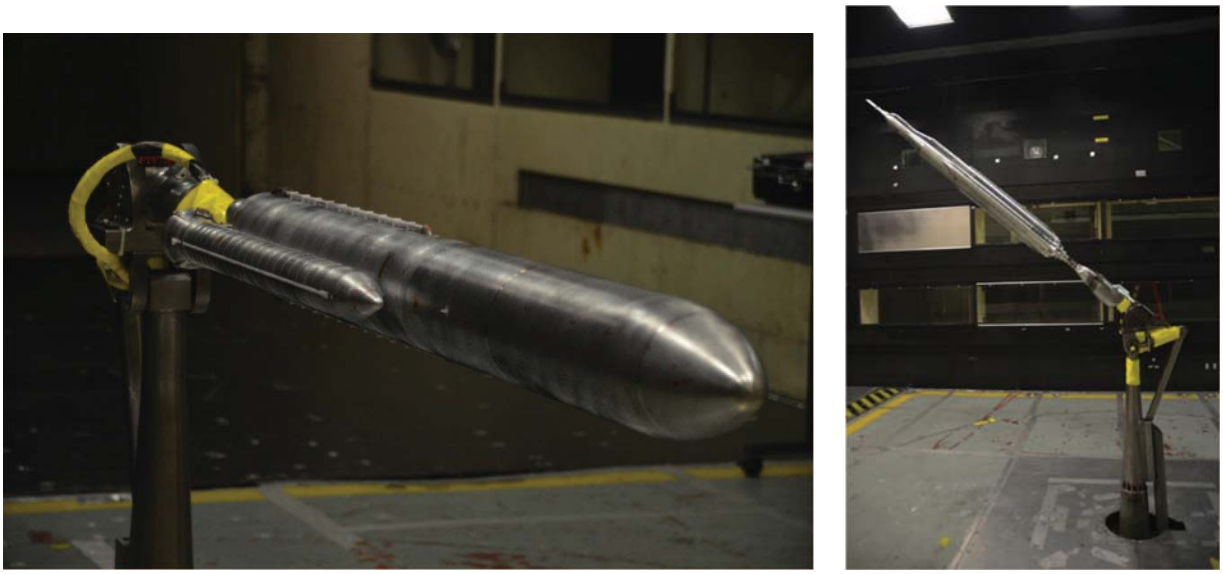

(a) (b)

Figure 7. Pictures of wind tunnel models: (a) SLS-27000 model in the 0° angle of attack position with the pitch adapter in the 0° offset position, and (b) SLS-10000 model in the 45° angle of attack position with the pitch adapter in the 45° offset position.

The SLS models were sting-mounted on the facility's vertical support post. Sting 350-39 is a 39-inch long, 1.5-inch diameter sting, made of Vascomax 350 stainless steel. The sting is mounted to a motorized roll coupler that allows for 360° of continuous vehicle roll capability. Vehicle roll angle is denoted in this paper by ϕ. The roll coupler was mounted to a custom 45° pitch offset adapter that was fabricated for the Ares I test and re-used for the SLS test. This adapter could be set to two positions: 0° and 45°. With a 55° pitching motion range, the vertical post system allowed for testing at a total angle of attack range from -10° to +45° with the pitch adapter in the 0° offset position, and from 35° to 90° with the pitch adapter in the 45° position. This allowed for an overlap of 10° between both pitch sweep types to ensure that there were no bias effects between the two setups. When the model was at a 90° attitude, the center of the model was approximately at the center of the test section. The vertical motion of the vertical strut allowed for the model to remain as much as feasible in the center of the test section. Figure 7(a) shows the SLS-27000 model in the 0° position, and Fig. 7(b) shows the SLS-10000 in the 45° offset position.

3. Tower Interference Testing Setup

Figure 8 shows the orientation of the vehicle with respect to the launch tower and mobile launchpad, and with respect to the true north geographical direction. The launch tower is located to the north of the launch pad complex. Therefore, a north wind ($\psi = 0°$) blows through the tower and onto the bottom side of the vehicle imparting a positive normal force. A south wind ($\psi = 180°$) blows onto the top side of the vehicle and then through the tower, imparting a negative normal force on the vehicle. West winds ($\psi = 270°$) would impart a positive side force, and east winds ($\psi = 90°$) would impart a negative side force on the vehicle. In this setup, by definition, the vehicle roll angle with respect to the wind, ϕ, happens to coincide with the wind azimuth angle, ψ, as seen in Fig. 8.

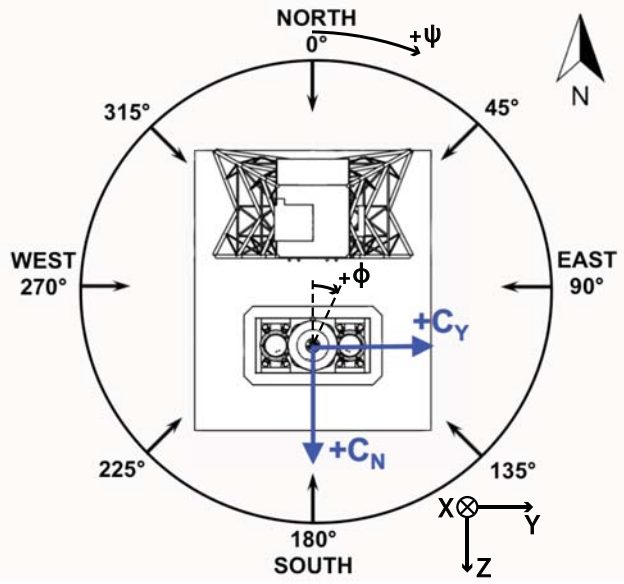

Figure 8. Top view of the SLS vehicle on the launch pad with definition of wind azimuth angles, and positive normal and side force directions.

Tower interference effects are required for ground winds coming from all azimuthal directions, ψ, when the launch vehicle is at various heights with respect to the tower, from $h/L = 0$ to $h/L = 1$, to simulate the vehicle lifting off until it clears the tower. The vertical movement of the post could only physically allow for a maximum h/L of 0.94. At that height, only a small portion of the SLS vehicle is affected by the tower and an extrapolation to zero-interference at $h/L = 1.20$ from the value at $h/L = 0.94$ was used to fulfill the requirement. The main support system was mounted on the facility cart turn-table that has a rotating capability of $\pm 165°$, for a total range of 330°, which results in a gap in wind azimuth angles that can be obtained in the tunnel. Because the model and tower are close to being symmetric about the X-Z plane, the model was mounted such that the 30° azimuth portion where data could not be acquired was placed for winds coming from the $\psi = 70°$ to 110° azimuth angles, i.e., east winds. To fill in the data gap, the plan was to use the westerly winds data acquired for the 250° to 290° azimuth angles and use symmetry assumptions. This ensured that the most important orientations, north and south winds, were able to be acquired. Data was taken in both positive and negative azimuthal directions in increments of 15°. Positive azimuth sweeps therefore started at $\psi = 110°$ increasing to $\psi = 360°$ and then following through to $\psi = 70°$, and a negative azimuth sweep started at $\psi = 70°$ decreasing to $\psi = 0°$ and following through all the way down to $\psi = 110°$.

To compute tower interference effects in an incremental fashion, data needed to be acquired without the launch tower, and then with the launch tower. The difference between the two constitute the tower effect increment. Azimuth sweep data was acquired first without the tower and mobile launchpad, as seen in Fig. 9(a). Theoretically, because of the absence of the tower, the height of the model should not matter. In order to check for data quality and consistency, and to provide statistics data for the uncertainty analysis, full azimuth sweeps were performed at various h/L heights. Once all 4 configurations were tested, the tower and mobile launchpad were installed, and identical sweeps were performed again but this time with the tower interference effects. Figure 9(b) shows the SLS-28000 configuration in this testing mode at a mid-level height. Figure 10 shows schematics of the four configurations tested in relation to the launch tower.

D. Instrumentation, Measurements, and Data Acquisition

The models were equipped with both a six-component integrated aerodynamic load measurement device, NASA Langley balance 756 and three ESP modules for measuring a small number of surface pressures. In general, force and moment aerodynamic testing is performed separately from other tests such as surface pressure testing. The main reason for this is because it can be difficult to route instrumentation cables through a force and moment model that typically requires bridging the balance to route the cabling to the

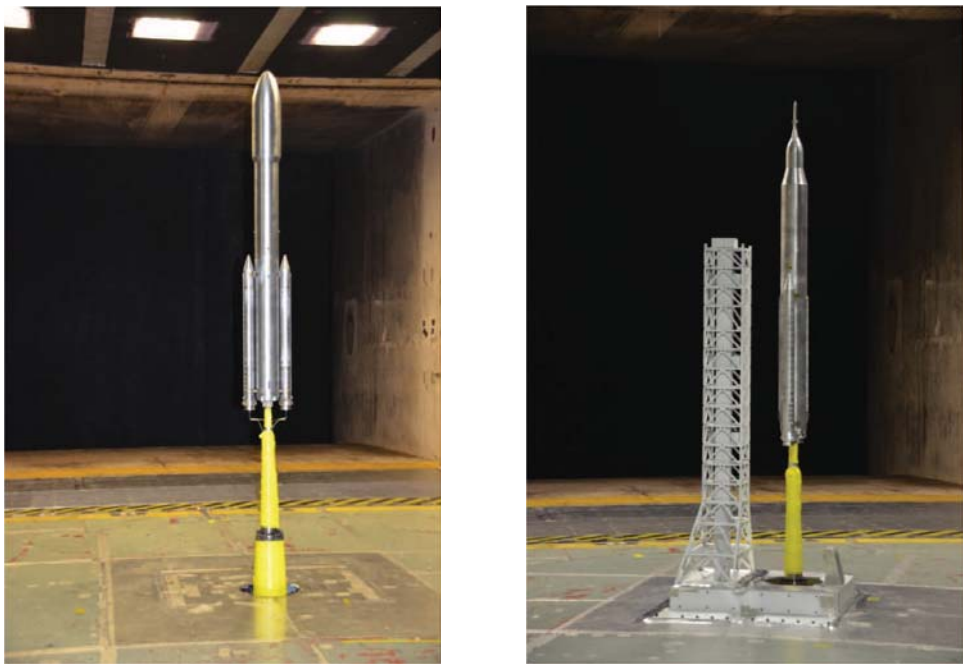

(a) (b)

Figure 9. Pictures of wind tunnel models: (a) SLS-21000 configuration in the tower effects testing setup mode without the tower, and (b) SLS-28000 configuration in the tower effects testing setup mode with the tower and mobile launchpad.

data acquisition equipment. Bridging of the balance is usually not recommended since it could introduce a load path between the metric part of the balance (the front end) and the non-metric part of the balance (the back end) that would not be accounted for. In the present case, because of the large model size and the small number of cables that were necessary for the surface pressure measurements, it was determined that the interference due to the cables on the load measurements would be very minimal, if at all measurable. At the outset of the test, a verification of this assumption was accomplished and it was indeed found that no measurable difference could be detected in the load measurements between before connecting pressure cables and after connecting them.

1. Coordinate Systems

The standard SLS coordinate system used to post-process wind tunnel data and create aerodynamic databases is the body axis system, in which all forces and moments are tied to the vehicle in all degrees of freedom. For the transition part of testing, the aerodynamic data is however acquired in pitch and roll sweeps. The data is therefore acquired in the missile axis system but then transferred to the body axis system. Figure 11 describes both of these axis systems.

2. Force and Moment Measurements

The primary force and moment strain gauge balance used during the test was NASA Langley balance 756. Figure 12 shows a picture of the balance. The backup balance was NASA Langley balance 755. Both are very similar balances and were calibrated in May 2013, just before the wind tunnel test. They are 1.375-inch font-end-expander type balances with a normal force capability of 2000 lbf. These balances were chosen for this test based on their load range that seemed appropriate in relation to the load estimates calculated pre-test. It is always desirable to use the maximum amount of the balance load capability in order to increase the accuracy of the measurement. It was however not predicted before the test that significant model dynamics would be encountered. These issues are described and discussed in detail in Section II. The smaller the balance diameter, the higher the deflections for a given applied load, i.e., the more flexible the balance. One of the lessons learned from this test was that a larger diameter, stiffer balance would have

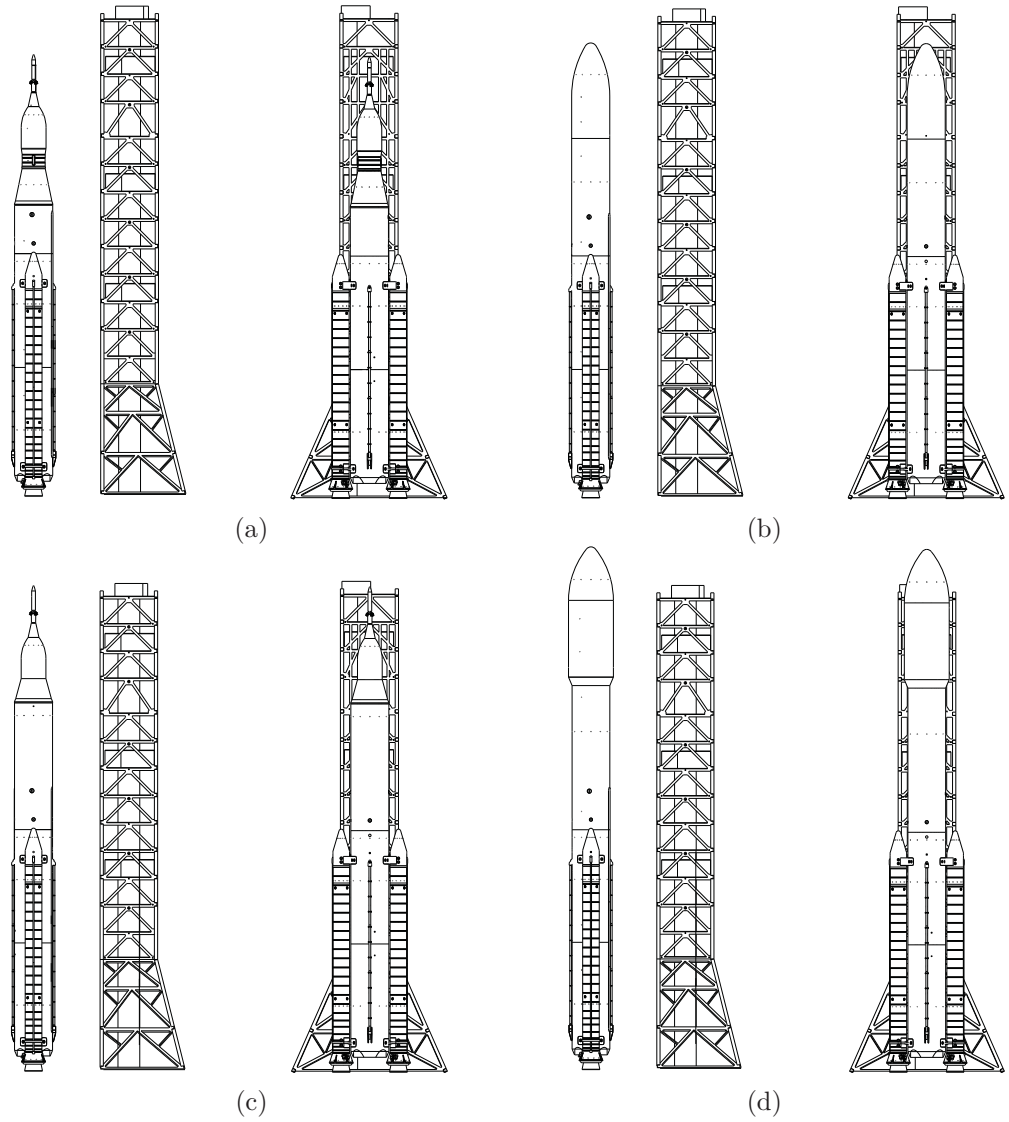

Figure 10. Side and front views of (a) SLS-10000, (b) SLS-27000, (c) SLS-28000, and (d) SLS-21000.

been more beneficial for acquiring data in the zones of high-dynamics, even though the accuracy might have been just slightly lower.

The balances are equipped with three platinum resistance thermometers (PRT) that allow for a highly accurate measurement of the balance temperature at three locations: forward, center, and aft. These temperatures are monitored continuously during the length of the test for two reasons: the overall temperature has to stay below 180 °F, and the temperature gradient through the balance (i.e., the temperature difference between forward and aft PRT measurements) should stay below 10 °F. The balance excitation voltage of 5 V is also monitored continuously to ensure that there is no drift in the excitation and therefore, potentially in the measured aerodynamic coefficients. The sting-to-balance fit was inspected prior to the test with 100% surface contact between the balance taper and the front end of the sting. Custom balance keys were fabricated to ensure a perfect fit between the balance and the sting, ensuring that no play would exist in the support hardware.

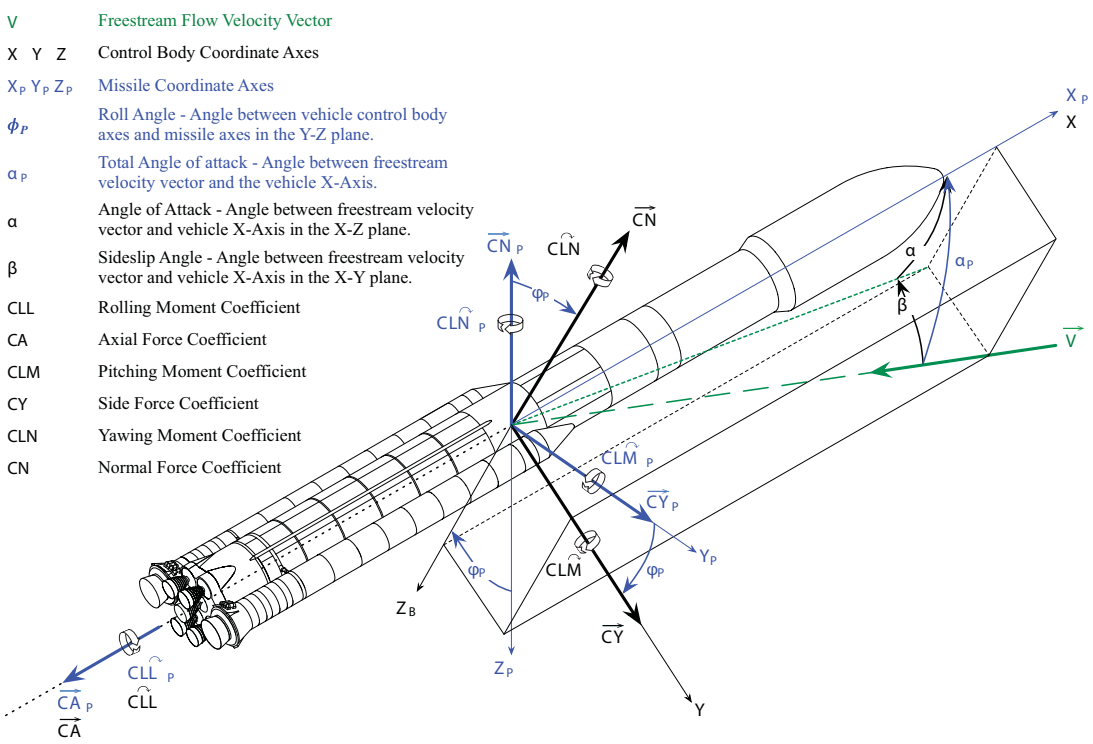

Figure 11. Definition of the SLS body axis system and the missile axis system

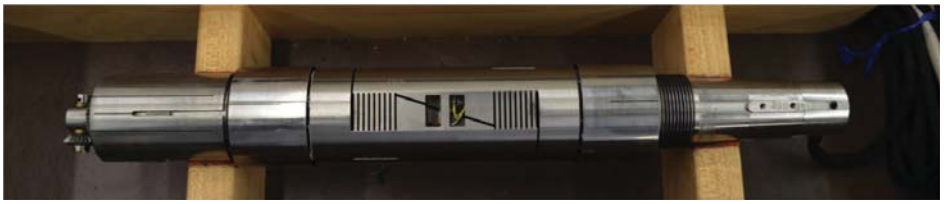

Figure 12. NASA Langley Strain Gauge Balance 756; front balance expander is on the left side, and sting taper on the right.

3. Base Pressure Corrections

Because the core main engine and SRB plumes were not simulated in the wind tunnel, the base pressure that is experienced by the vehicle in flight is vastly different than the base pressure measured in the experiment. The flight base pressure aerodynamic database is a separate product that is developed from historical data and very specialized ground tests. The base pressure in the wind tunnel test is therefore measured at the base of the core stage and both boosters, and a base force is calculated using the base area of each body. The base force is then removed from the axial force coefficient, C_A. Similarly, due to the off-centerline booster configuration, a yawing moment could be created from a differential pressure measured on the right and left boosters. A base yawing moment coefficient is therefore also calculated and removed. Both of these corrections result in forebody forces and moments. All aerodynamic coefficients reported in this paper are forebody forces and moments, with base forces and moments removed. Figure 13 shows a view of the base of the wind tunnel model. The base was equipped with four independent base pressure measurements. These measurements were acquired and averaged to compute the base force on the core stage. Each SRB was equipped with two independent base pressure tubes that were also averaged in order to compute the SRB base pressure force and moment.

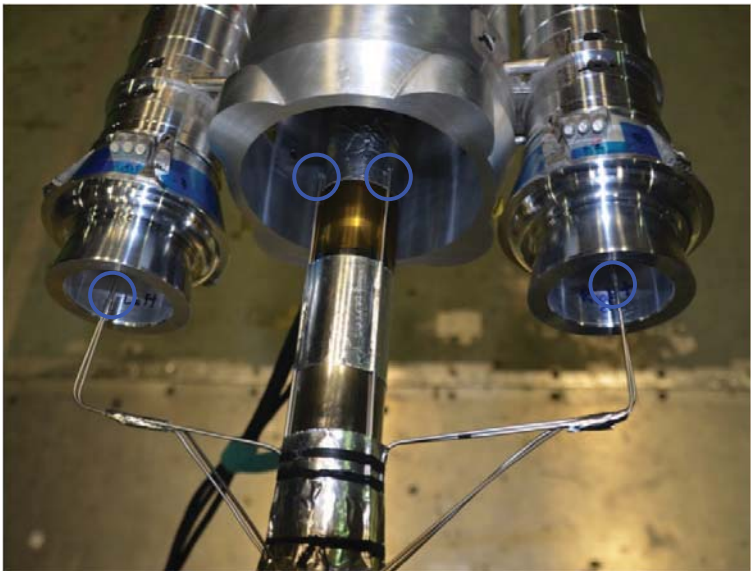

Figure 13. View of the base of the wind tunnel model with base pressure tube-ends identified by blue circles.

4. Surface Pressure Measurements

A set of 154 surface pressure taps were drilled into the model during fabrication and then instrumented and connected to three ESP modules, one per body (two boosters, one core). The lower part of the core stage contained 34 surface pressure measurements, each booster contained 46 surface pressure measurements, and each different nose contained 28 surface pressure measurements. The main goal of acquiring a limited set of surface pressures on the vehicle was for CFD validation and anchoring. Carlson et al.[6] and Krist and Ghaffari[5] discuss the use of the experimental surface pressures to help calibrate the distributed aerodynamics reduced-order model that was derived from CFD alone. Results from the surface pressure measurements will not be discussed in this paper.

5. Model Attitude Measurements

For the tower interference testing phase, the model was always at a total angle of attack of 90°. The wind azimuth angle and model roll angle were determined directly from the facility turn table encoder output. For the transition testing phase, model attitude angles (pitch and roll) were acquired in two different ways. The primary model attitude measurement was based on a calibration of the vertical post strut adapter using a high precision accelerometer. Model attitude was then calculated based on misalignment angles of the sting, balance, and model, measured during installation, and based on sting/balance deflection measurements completed during the balance calibration phase. This is the traditional and most precise way of knowing the model attitude in a wind tunnel. The secondary attitude measurement was an onboard three-accelerometer device that allowed for a direct measurement of the model attitude angles based on an offline calibration procedure. Several issues were encountered with the method, even though for most of the test duration, this measurement was very consistent with the calculated attitude. One of the issues was that model dynamics and vibrations introduce noise in the measurement (also known as sting whip). The other issue was that when the model is at high total angles of attack ($\geq$70°), this type of measurement becomes imprecise, and does not allow for a measurement of roll angle at a total angle of attack of 90°.

II. Test Results and Discussion

The NASA LaRC 14x22 SWT Test 609 was conducted from July 15^{th} to August 14^{th}, 2013, with 242 occupancy hours, and 88 wind-on hours. A total of 224 runs were completed, and over 3700 data points acquired. As previously mentioned, the sting/balance system that was chosen was more flexible than desired, and though it was an appropriate choice for most of the test matrix where the vehicle did not

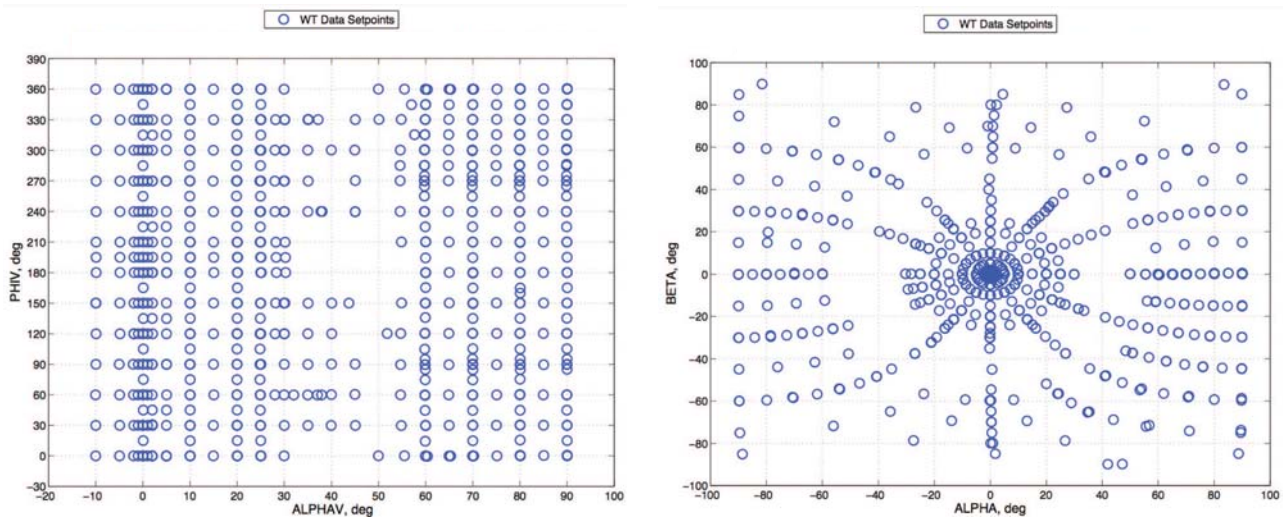

(a) (b)

Figure 14. Wind tunnel dataset for the transition testing portion of the SLS-10000 configuration in (a) the α_V, ϕ_V space, and (b) the α, β space.

encounter significant dynamics, it was not an appropriate choice for the areas where significant dynamics were experienced. The magnitude of the model dynamics was highly sensitive about pitch angle α_V, roll angle ϕ_V, and configuration. For instance, the SLS-21000 configuration did not experience the magnitude of dynamics that the SLS-10000 did. During transition testing, the strong sinusoidal excitations of the model always occurred in the mid-range angles of attack (from $\alpha_V = 30^\circ$ to $\alpha_V = 60^\circ$). When the dynamics occurred, the flow was quickly dropped and the angle of attack lowered by the facility test team to dampen out the model oscillations and avoid overloading the sensitive strain gauge balance, or damage the model. Figure 14 shows the dataset acquired for the SLS-10000, as a function of α_V and ϕ_V on the left, and as a function of α and β on the right.

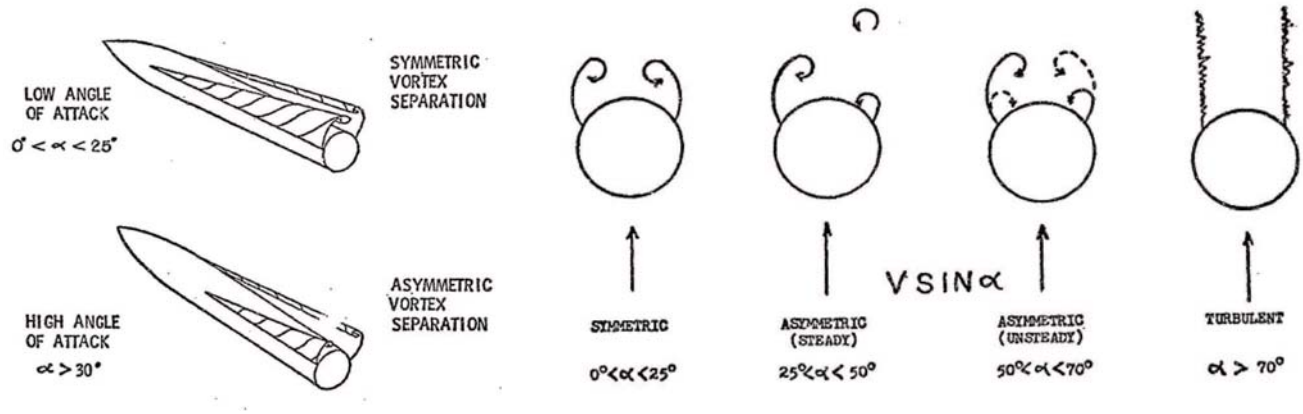

Figure 15. Schematics describing the steady asymmetric vortex shedding experienced at high angles of attack on slender bodies. From Kubin[8] (1973).

It can be noticed in these figures that the dynamics issue resulted in a sparser dataset in the mid-range angles of attack, which made the subsequent development of the aerodynamic database more challenging. The database development work will be described in a future article. In the same α_V range where the dynamics were encountered, the data showed significant lateral loading. Though difficult to predict, it is a well known phenomenon in the missile and slender body aerodynamics community that a steady asymmetric vortex pattern can lock-in between approximately $\alpha_V = 30^\circ$ and $\alpha_V = 60^\circ$. Kubin[8] published a study on steady asymmetric vortex shedding on slender missiles in 1973, and showed evidence of the physical phenomenon.

Two of his schematics in Fig. 15 illustrate the difference in the vortex shedding process as a function of angle of attack. Below 25° angle of attack, the vortex shedding is very symmetric and mostly attached. Between 25° and 50°, the vortex shedding becomes strongly asymmetric in a steady fashion, i.e., the strong vortex remains on the same side, once it is established. From 50° to 70° angle of attack, the asymmetric shedding becomes very unsteady and starts alternating from side to side at a predictable Strouhal frequency. Above 70° the shedding becomes turbulent, and a turbulent shear layer develops on each side of the slender body. Kubin's findings, though applied to a simple slender body of revolution, seem to coincide with our findings on a more complex launch vehicle configuration. The range of angles where the steady asymmetric vortex occurred is very consistent with those findings. The CFD simulations that were run in parallel to the wind tunnel test are also an indication that steady asymmetric vortex shedding does occur on this vehicle. Krist and Ghaffari[5] were able to predict this phenomenon with a detached eddy simulation (DES), although the vortex was sometimes predicted on the opposite side than observed in the wind tunnel. At the end of the wind tunnel test, a smoke flow visualization study was conducted to attempt to better understand the nature of the flow around the tower and in its wake as its shear layers impinge on the launch vehicle when the winds are from the north. Figure 16 shows two photos of the seeding smoke following the flow streamlines and curving around the launch tower. A significant amount of downwash is shown on the leeward side of the tower, and the flow exhibited many unsteady features.

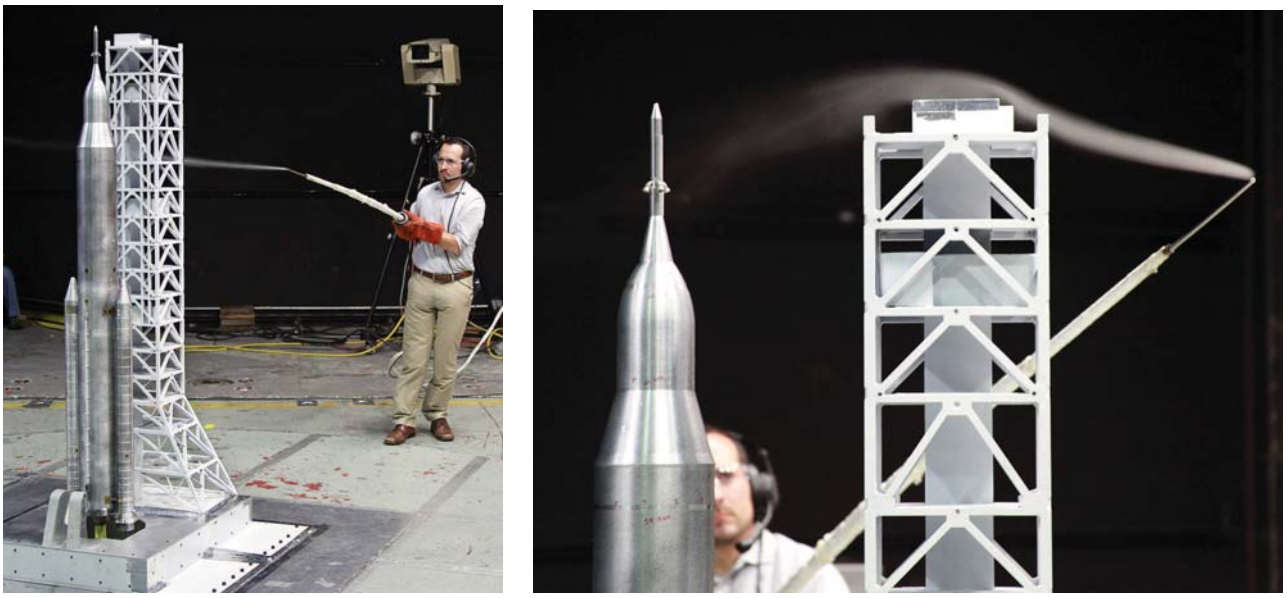

Figure 16. Smoke flow visualization performed to investigate the nature of the flow around the launch tower, between the launch tower and the vehicle, and in its wake.

Due to the large amount of data collected, only a small representative number of data plots can be shown in this conference paper. A comprehensive report with all of the test data is being written as an internal NASA report/SLS document, and will be available as an ITAR/SBU protected document in the near future. The following plots show forebody forces and moments in the body axis system as a function of α_V (ALPHAV) for pitch sweeps, and ϕ_V (PHIV) for roll sweeps. The error bars shown only account for balance calibration uncertainty, it should therefore be interpreted as a minimum uncertainty.

Figure 17 shows the aerodynamic coefficients for 10 pitch sweeps at a roll angle of $\phi_V = 0°$ for the SLS-10000 configuration (C1). Five of these runs are repeat pitch sweeps at the lower angles of attack, and the other five are repeat pitch sweeps at the higher angles of attack. With the goal of ensuring data quality throughout the test, repeatability assessments were performed at regular intervals during the test and were of two different types:

1. A reference set of runs was acquired initially and then at regular intervals during the test to ensure data consistency throughout the entire length of testing. Any long-term unexpected change in flow quality or any balance issue would be uncovered and investigated before any additional production

runs were performed.

2. Uncertainty assessment repeat runs were also performed throughout the test to capture the dependency of data repeatability with all the variables. During post-processing, statistical methods are used to quantify repeatability, as used by Hemsch et al.[9] and Houlden et al.,[10] and following processes described by Montgomery.[11] It is therefore important to gather repeatability data at various attitudes and flow conditions to detect any correlation in the residuals, in which case an uncertainty model can be built using this information.

Balance calibration uncertainty is a result of the statistical curve fit error produced during balance calibration in the laboratory. It is therefore known before starting a test. For both types of repeats cited above, balance calibration uncertainty is used in real time as a measure of minimum uncertainty. Therefore, two repeat runs that do not fall within the balance calibration uncertainty bounds are not necessarily bad repeats, however, best practices and experience with these six-component balances has shown that discrepancies between repeats should be expected to be either within the balance calibration uncertainty or on the same order of magnitude.

Figure 17 shows multiple repeat pitch sweeps, as do many of the plots shown in this paper. Since absolute magnitudes are not provided, the reader should focus on the magnitude of the discrepancies between repeat measurements relative to the total variation over a run and the magnitude of the balance calibration uncertainty represented by the error bars. In general, data quality was found to be very satisfactory. The area where repeat residuals were the highest was in the mid-range angles of attack.

It is clear that there is a gap of data where dynamics were too high to be able to acquire data. The asymmetric loading is evidenced at around $\alpha_V = 30°$, where the runs don't all collapse. This appears to be a very high gradient area with potentially several possible states for a given attitude. Even though these pitch sweeps were conducted at $\phi_V = 0°$, where lateral loading should be minimal, there clearly is a significant effect of the lateral loading on the side force and yawing moment trends in the mid-range angle of attack range. Similarly, Figs. 18 and 19 show similar plot of pitch sweep runs at $\phi_V = 30°$ and $\phi_V = 60°$, respectively. At those angles, it should be anticipated that lateral forces and moments would be loaded because of the presence of the large SRBs. Again, the mid-range angle of attack range is highly non-linear. Figure 20 shows a series of entire roll sweeps from $\phi_V = 0°$ to $\phi_V = 360°$, at various pitch angles from $\alpha_V = 0°$ to $\alpha_V = 90°$.

Figures 21, 22, and 23 show pitch sweeps at $\phi_V = 0°$, $\phi_V = 30°$, and $\phi_V = 60°$, respectively for the SLS-27000 configuration (C23). At $\phi_V = 0°$, a small amount of dynamics was encountered that prevented overlap in the mid-range angles of attack, however, this configuration was found to be much more stable. At $\phi_V = 0°$ and $\phi_V = 30°$, a nice overlap of 10° was achieved and found to be very consistent between the two experimental setups.

Figures 24, 25, and 26 show pitch sweeps at $\phi_V = 0°$, $\phi_V = 30°$, and $\phi_V = 60°$, respectively for the SLS-28000 configuration (C25). This model was the most challenging for acquiring data in the mid-range angles of attack. There were large gaps of 35° over which data could not be acquired due to significant dynamics. A larger uncertainty will therefore be applied in this region due to the extra interpolation that will be required when building the aerodynamic database.

Figures 27, 28, and 29 show pitch sweeps at $\phi_V = 0°$, $\phi_V = 30°$, and $\phi_V = 60°$, respectively for the SLS-21000 configuration (C9). This model was surprisingly the best behaved from an aerodynamics standpoint. As seen in Fig. 27, repeatability is excellent, and overlap in the mid-range angles was close to perfect. Trends were also in general much less erratic than for SLS-10000, or SLS-28000.

Figures 30, 31, 32, and 33 show side force and normal force coefficients for tower interference testing of the SLS-10000, SLS-27000, SLS-28000, and SLS-21000, respectively. Each plot contains full azimuth sweep data for the vehicle at various h/L positions (specified by the HOL value in the plot legend), and with the tower present (TOWER = 1). Each plot also contains one full azimuth sweep without the presence of the tower (TOWER = 0), as a baseline. Very similar conclusions can be drawn from all four figures: the tower effect is maximum for winds from northerly directions ($\psi = 330°$ to $\psi = 30°$), and mainly affects normal force coefficient. At all other wind azimuth directions, the tower effect is small but always reduces the absolute value of the aerodynamic normal force. This is a favorable finding since, for south winds, the tower interference makes the normal force coefficient less negative, i.e., the winds don't push the vehicle as much toward the tower, which acts as blockage. For north winds, the tower interference makes the normal force coefficient less positive, i.e., the winds don't push the vehicle away from the tower as much as if the

tower was not there. The lightning protection system is located on the south side of the vehicle and is at an altitude of 500 ft. These results alleviate the concerns that the vehicle could impact the tower on its north side before it clears it, or could hit the lightning protection system on its south side before the launch vehicle clears 500 ft. Concerning side force coefficient, the tower effect is not as dependent on wind azimuth. It is however interesting to note that the presence of the tower increases the absolute magnitude of the side force coefficient at all azimuth angles. For a westerly wind, for example, the side force coefficient increases about 20% in absolute magnitude for $h/L = 0$. The tower acts as a porous flow-blocking object, which locally accelerates the flow between the tower and the vehicle, increasing the side force coefficient. As the vehicle lifts off and clears the tower, the tower effects vanish to zero and the launch vehicle is then only affected by the transition aerodynamic coefficients.

III. Conclusion

A comprehensive wind tunnel test was completed to characterize the liftoff aerodynamic environments and tower interference effects from ground winds of four variants of the SLS launch vehicle, the United States' future crew and cargo heavy lift launch vehicles. A large amount of experimental data was gathered covering the entire parameter space required for conducting flight simulations of the vehicle's liftoff event. This dataset was subsequently post-processed to develop an aerodynamic database that will be used to fly the vehicle for many decades to come. The opportune simultaneous gathering of surface pressure data enabled a unique data fusion investigation that resulted in a reduced-order model of the distributed surface quantities. A lesson was learned regarding the stiffness (or lack-thereof) of the sting/balance system that made data acquisition in the mid-range angle of attack range challenging for many of the configurations tested.

Acknowledgement

The authors would like to honor through this work the life of our dear friend and co-worker Noah Favaregh, who passed away too early. Noah was involved in the planning phases and early conduct of this wind tunnel test and had been a tremendous asset to our team for many years, not only because of his technical excellence, but also because of his generous personality, and kind spirit. We would also like to acknowledge the hard work performed by the NASA Langley 14- by 22-Foot Subsonic Wind Tunnel facility staff, engineers and technician throughout this test campaign, and the support by the Space Launch System program offices at the NASA Marshall Space Flight Center and at the NASA Langley Research Center, and the constant support from the SLS Aerodynamics Task Team.

References

[1]Blevins, J. A., Campbell, J. R., Bennett, D. W., Rausch, R., Gomez, R. J., and Kiris, C. C., "An Overview of the Characterization of the Space Launch System Aerodynamic Environments," *52nd Aerospace Sciences Meeting*, American Institute of Aeronautics and Astronautics, AIAA 2014-1253, 2014.

[2]Pinier, J. T., Bennett, D. W., Blevins, J. A., Erickson, G. E., Favaregh, N. M., Houlden, H. P., and Tomek, W. G., "Space Launch System Ascent Static Aerodynamics Database Development," *52nd Aerospace Sciences Meeting*, American Institute of Aeronautics and Astronautics, AIAA 2014-1254, 2014.

[3]Pritchett, V., Mayle, M., Blevins, J. A., Crosby, W., and Purinton, D., "Aerodynamic Tests of the Space Launch System for Database Development," *52nd Aerospace Sciences Meeting*, American Institute of Aeronautics and Astronautics, AIAA 2014-1256, 2014.

[4]Capone, F. J., Paulson, J. W., and Erickson, G. E., "Liftoff and Transition Aerodynamics of the Ares I Launch Vehicle," *Journal of Spacecraft and Rockets*, Vol. 49, No. 4, 2014/11/01 2012, pp. 564–573.

[5]Krist, S. E. and Ghaffari, F., "Results from CFD simulations of an SLS Variant at Liftoff Conditions with Comparison to Experiment," *AIAA Science and Technology Forum and Exposition (SciTech 2015)*, 2015.

[6]Carlson, H. A. and Verberg, R., "Reduced-order Model for NASA Space Launch Reduced-order Model for NASA Space Launch System Liftoff Aerodynamics," *AIAA Science and Technology Forum and Exposition (SciTech 2015)*, 2015.

[7]Gentry, G. L., Quinto, P. F., Gatlin, G. M., and Applin, Z. T., "The Langley 14- by 22-Foot Subsonic Tunnel: Description, Flow Characteristics and Guide for Users," *NASA Technical Paper 3008*, 1990.

[8]Kubin, J. S., *An Analysis of Steady Asymmetric Vortex Shedding from a Missile at High Angles of Attack*, Master's thesis, Air Force Institute of Technology, 1973.

[9]Hemsch, M. J., Hanke, J. L., Walker, E. L., and Houlden, H. P., "Detailed Uncertainty Analysis for Ares I Ascent Aerodynamics Wind Tunnel Database," *26th AIAA Aerodynamic Measurement Technology and Ground Testing Conference*, AIAA 2008-4259, 2008.

[10]Houlden, H. P., Favaregh, A. L., and Hemsch, M. J., "Quantification of the Uncertainty for the Ares I A106 Ascent Aerodynamic Database," *27th AIAA Aerodynamic Measurement Technology and Ground Testing Conference*, AIAA 2010-4926, 2010.

[11]Montgomery, D. C., *Introduction to Statistical Quality Control*, Third Edition, Wiley, 1996.

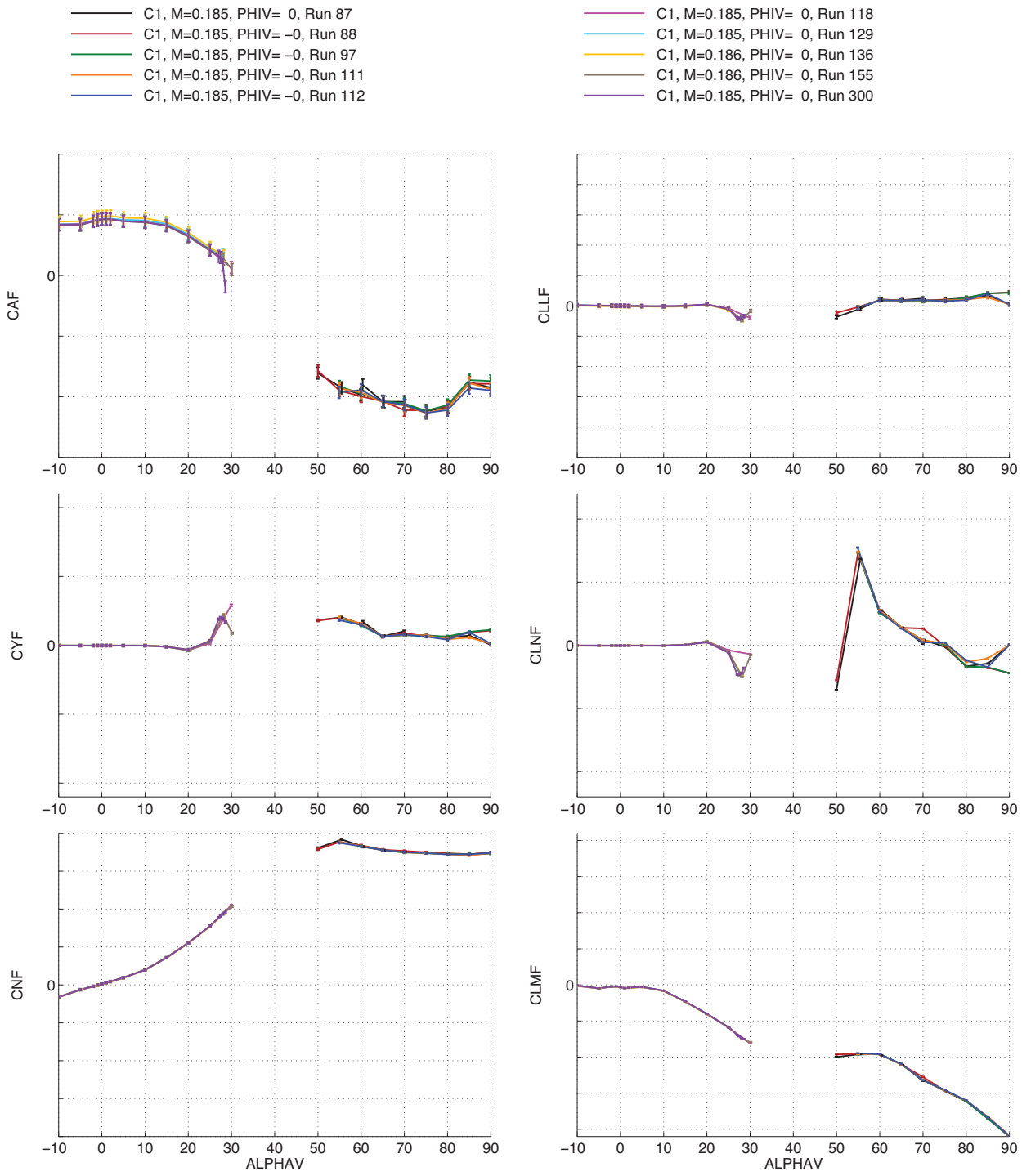

Figure 17. Aerodynamic coefficients for SLS-10000, pitch sweeps (with repeat runs) at $\phi_V = 0°$.

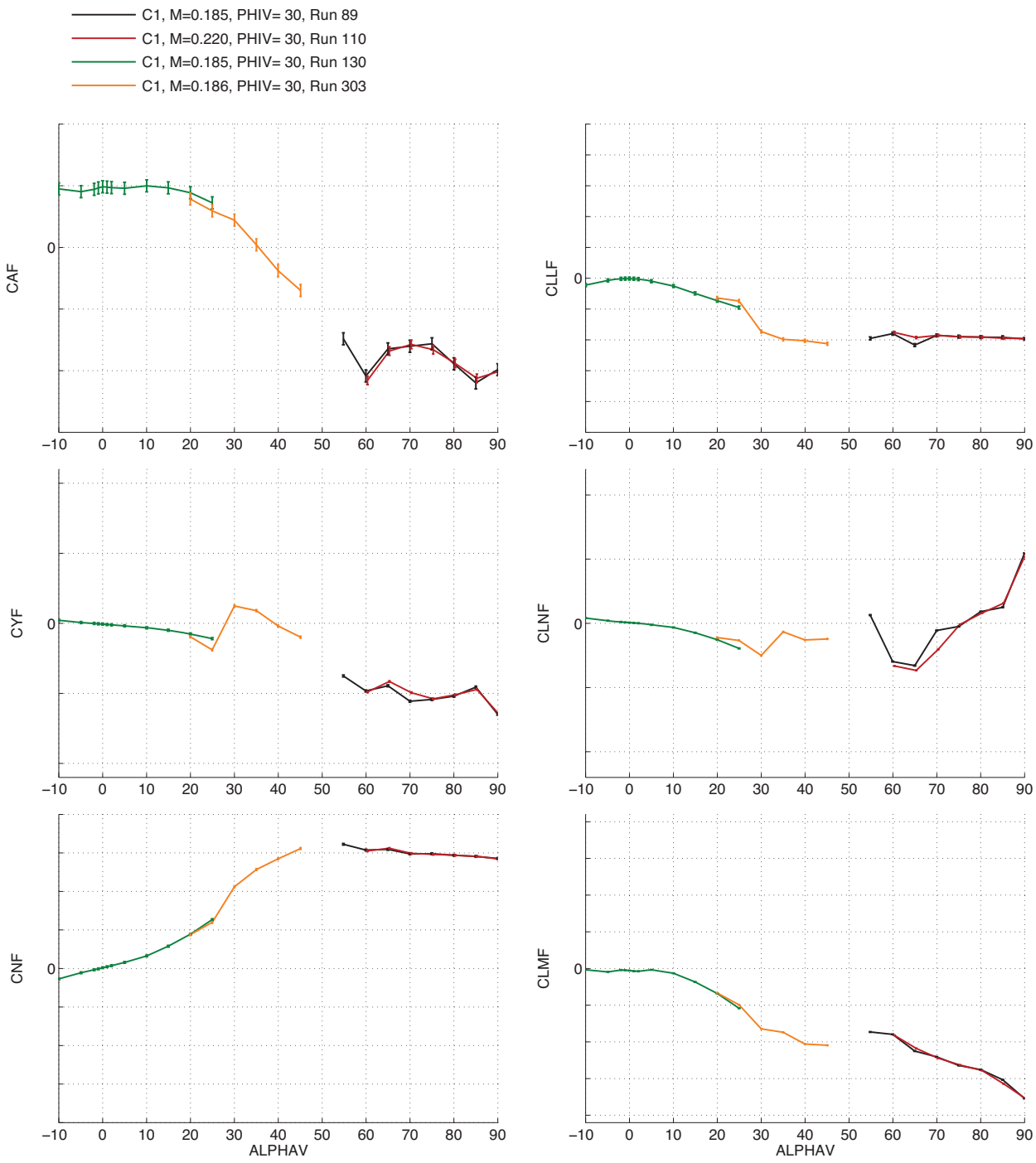

Figure 18. Aerodynamic coefficients for SLS-10000, pitch sweeps at $\phi_V = 30°$.

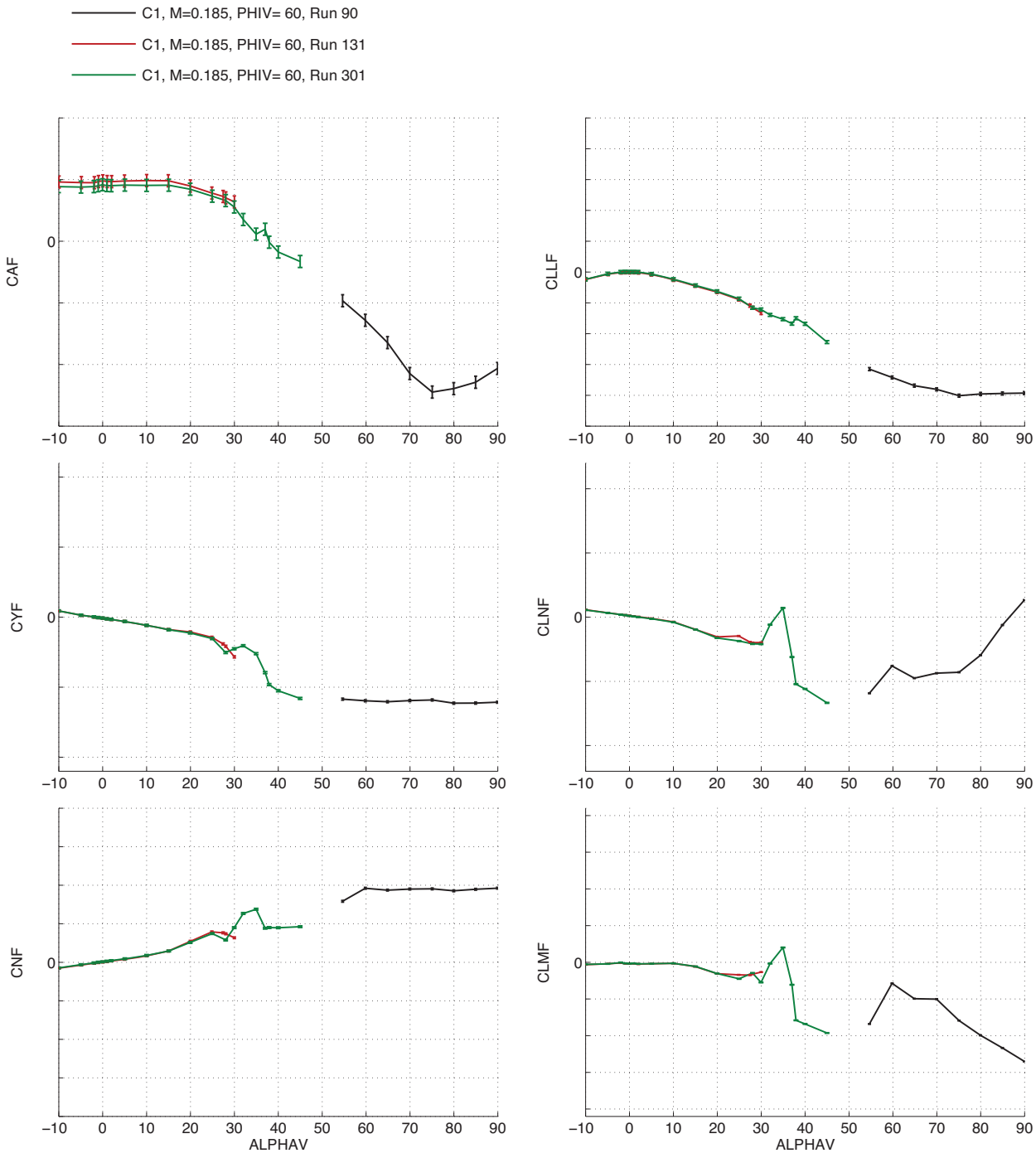

Figure 19. Aerodynamic coefficients for SLS-10000, pitch sweeps at $\phi_V = 60°$.

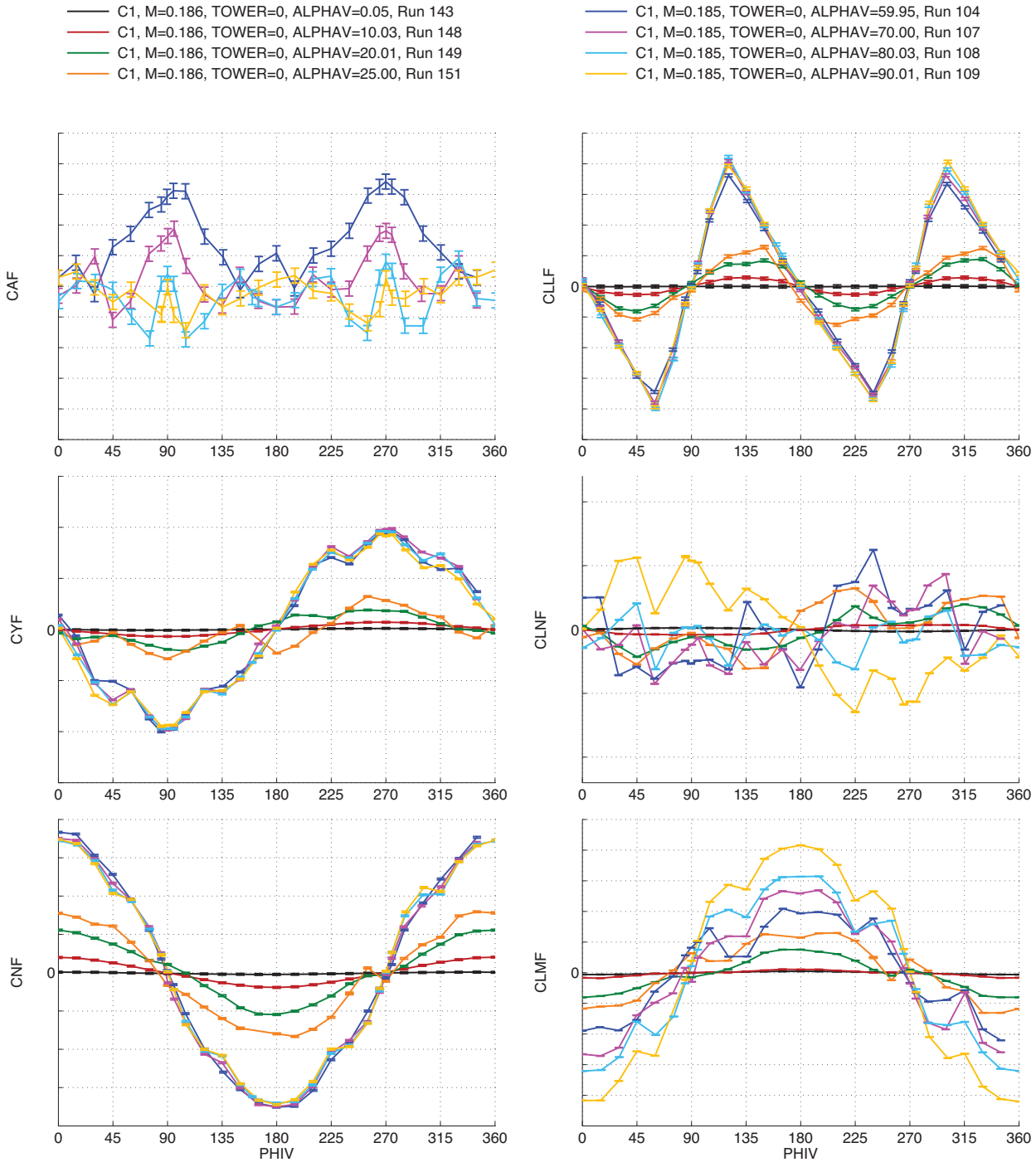

Figure 20. Aerodynamic coefficients for SLS-10000, roll sweeps.

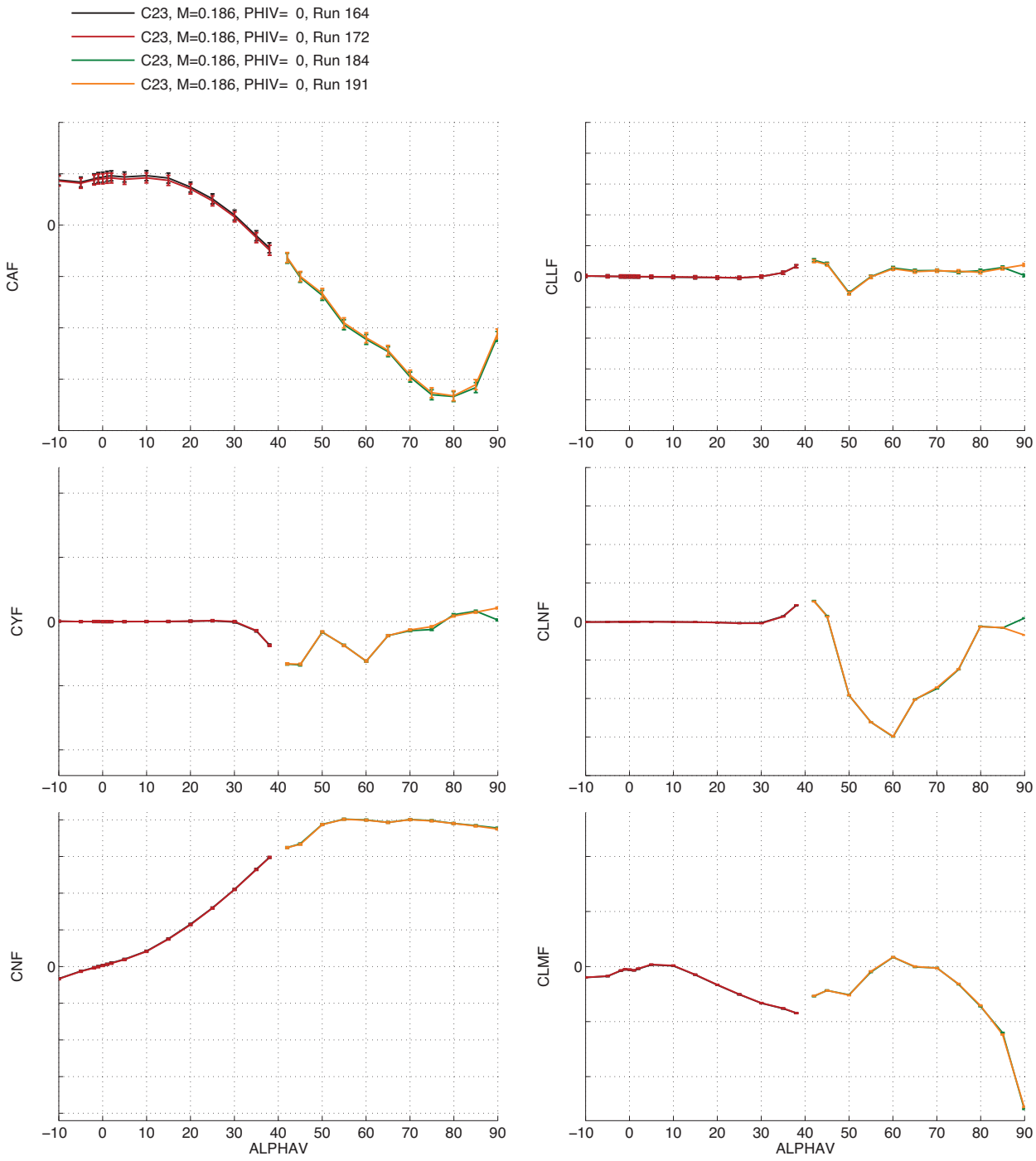

Figure 21. Aerodynamic coefficients for SLS-27000, pitch sweeps at $\phi_V = 0°$.

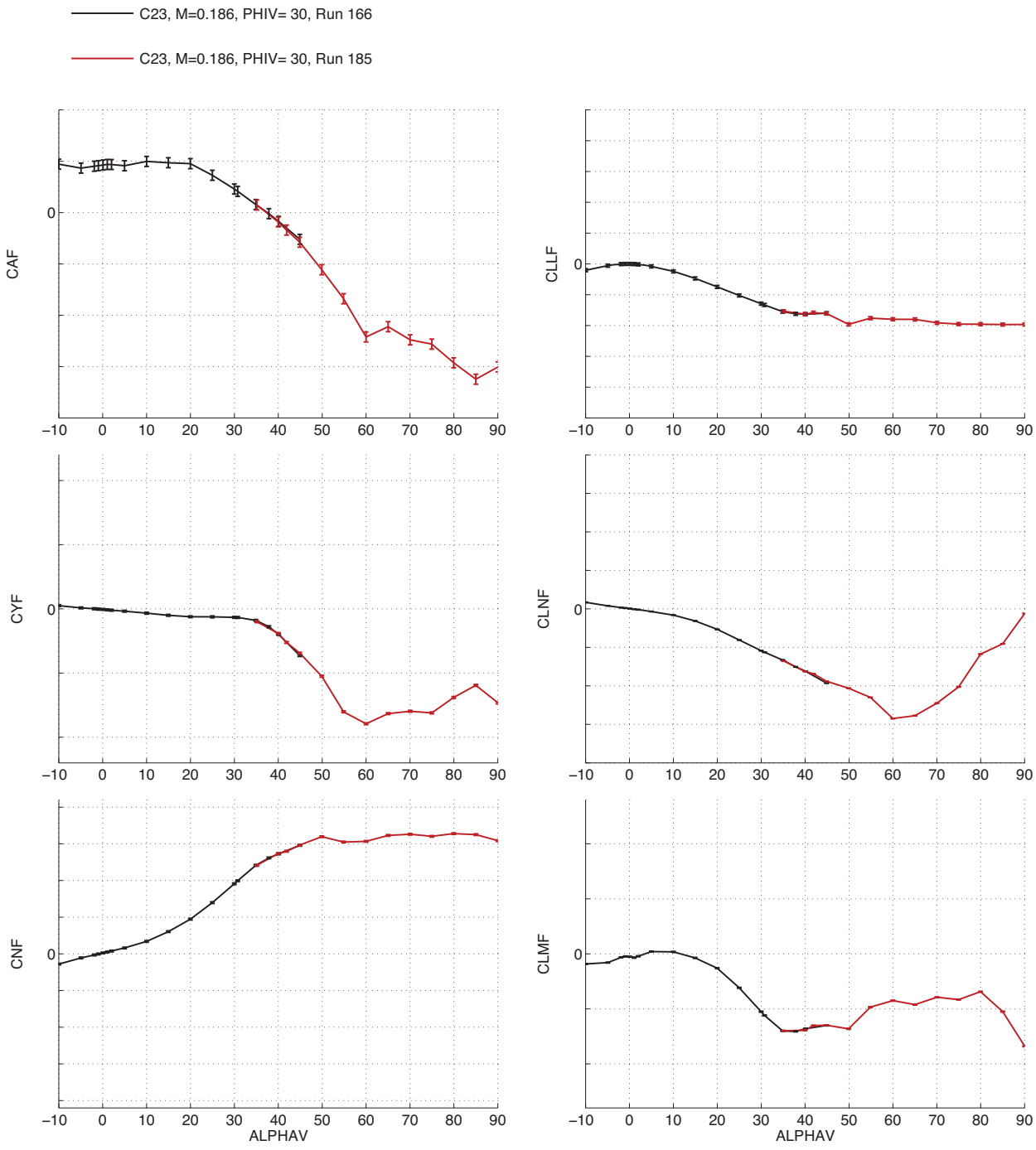

Figure 22. Aerodynamic coefficients for SLS-27000, pitch sweeps at $\phi_V = 30°$.

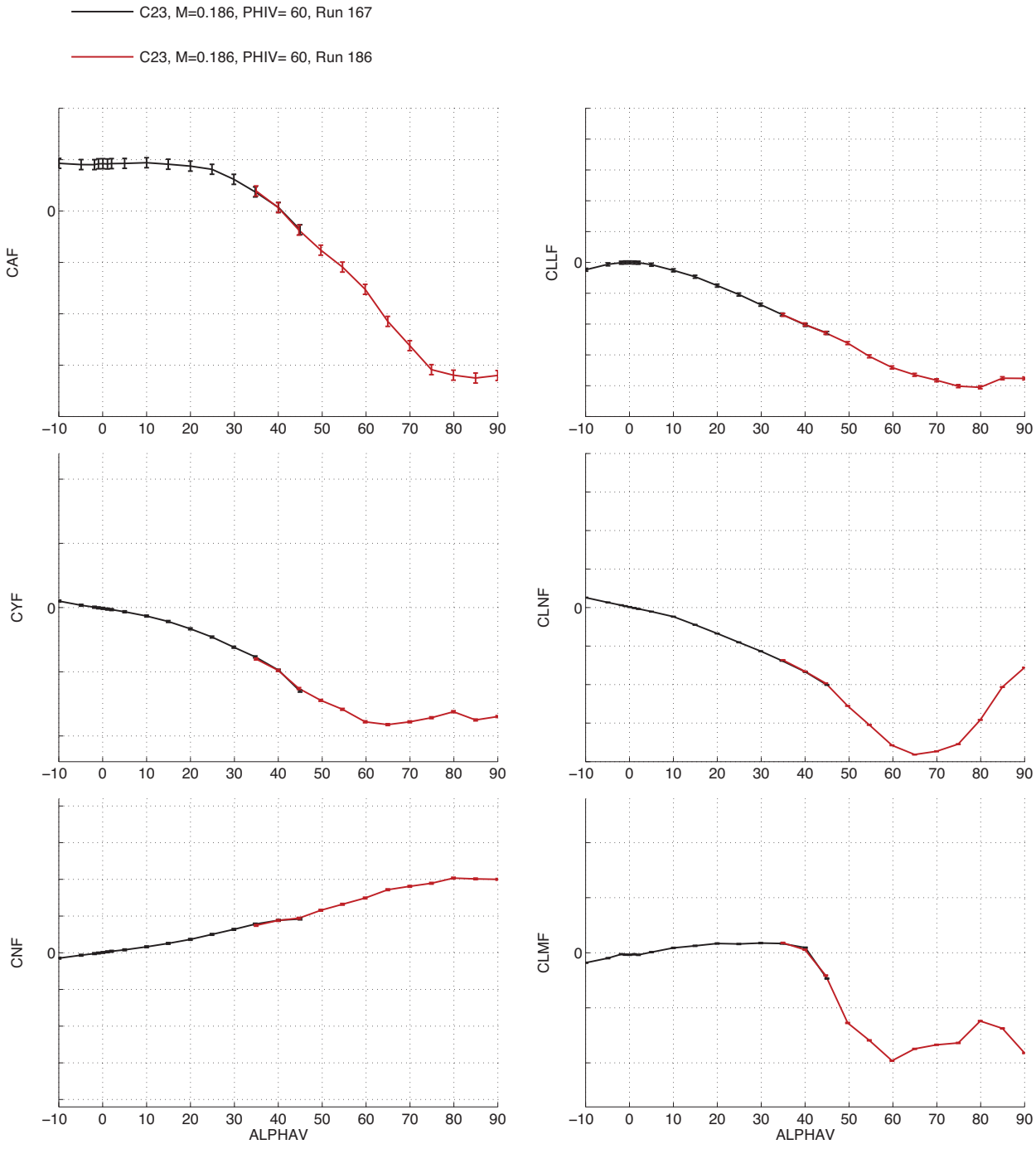

Figure 23. Aerodynamic coefficients for SLS-27000, pitch sweeps at $\phi_V = 60°$.

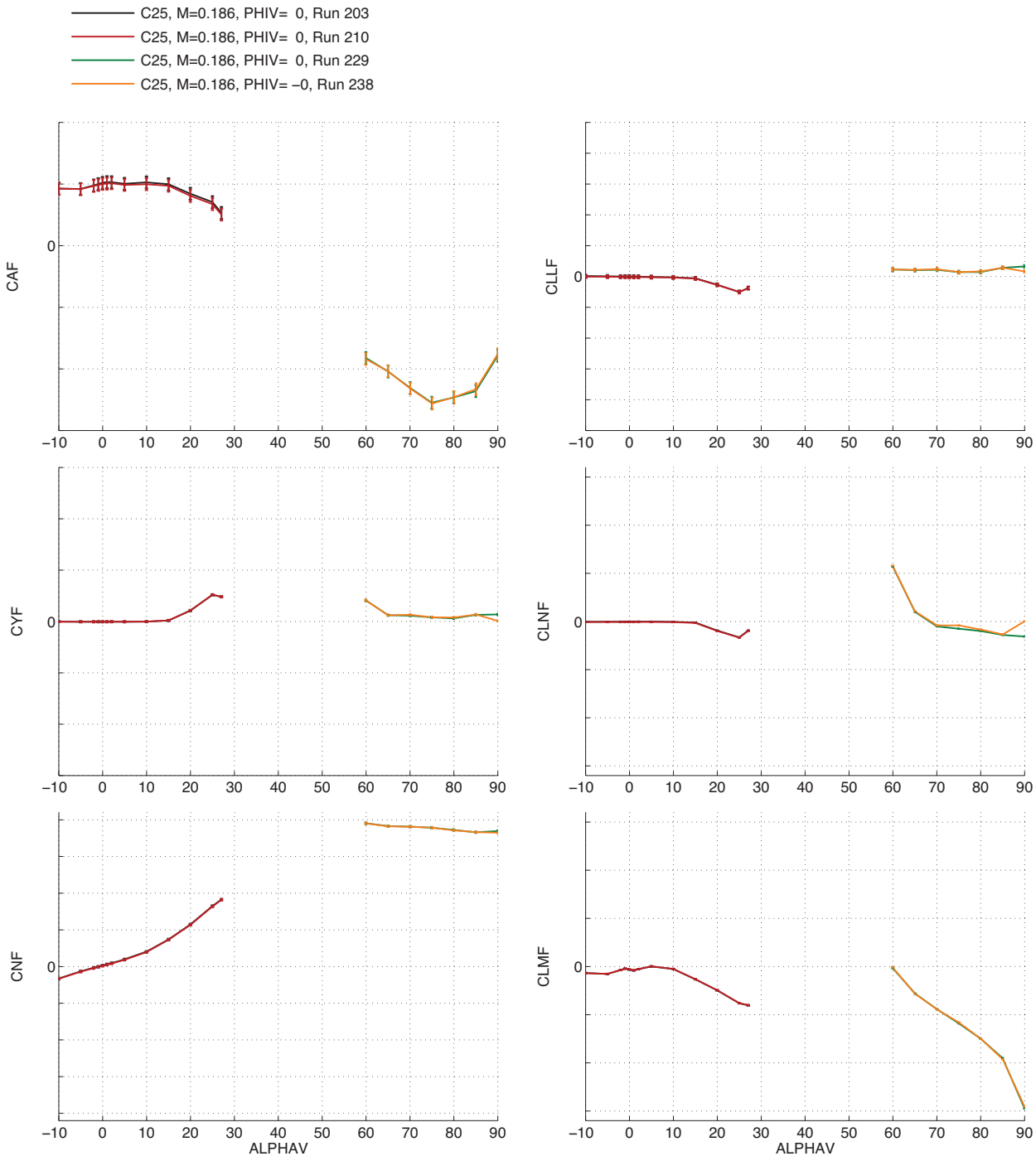

Figure 24. Aerodynamic coefficients for SLS-28000, pitch sweeps at $\phi_V = 0°$.

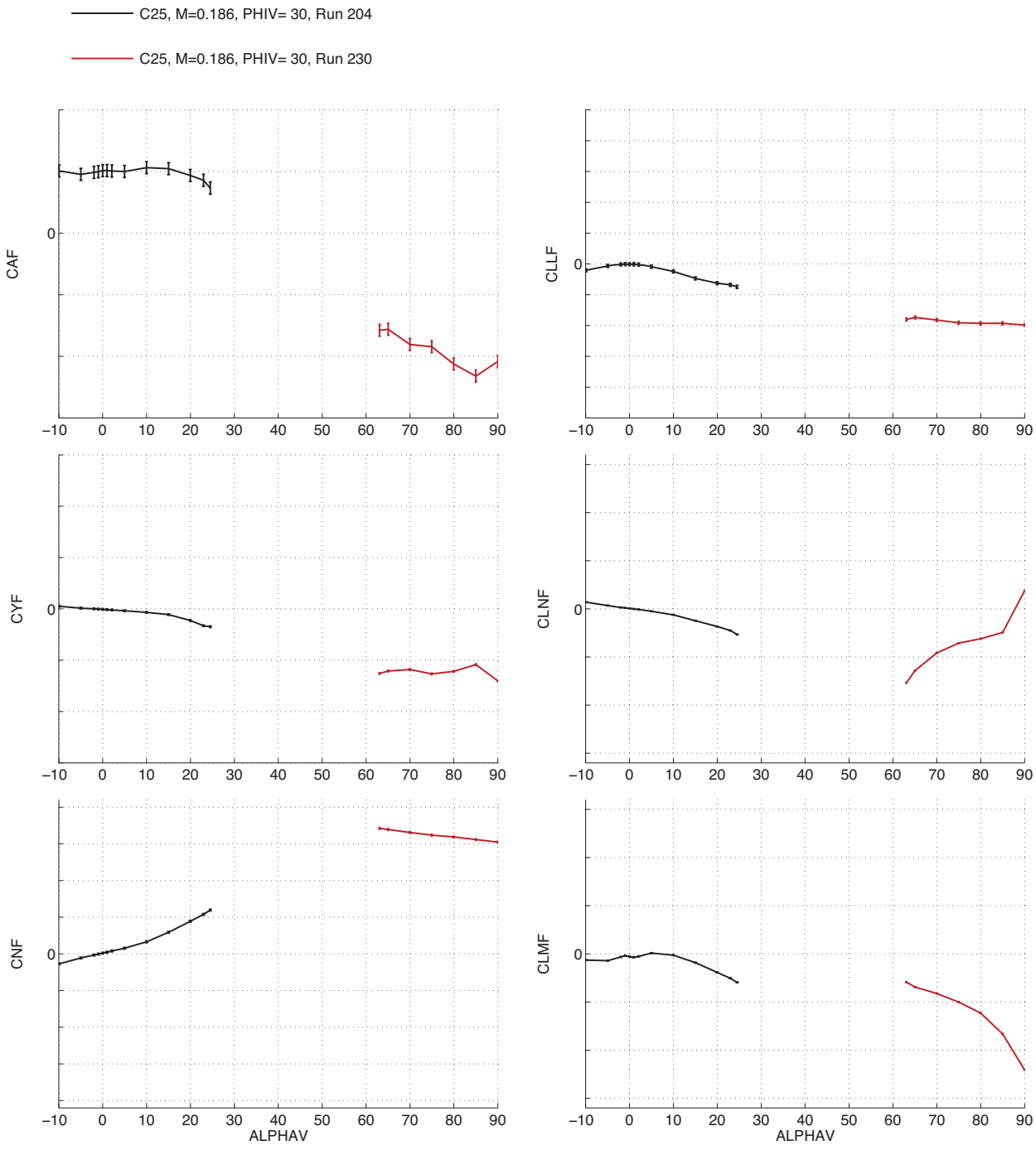

Figure 25. Aerodynamic coefficients for SLS-28000, pitch sweeps at $\phi_V = 30°$.

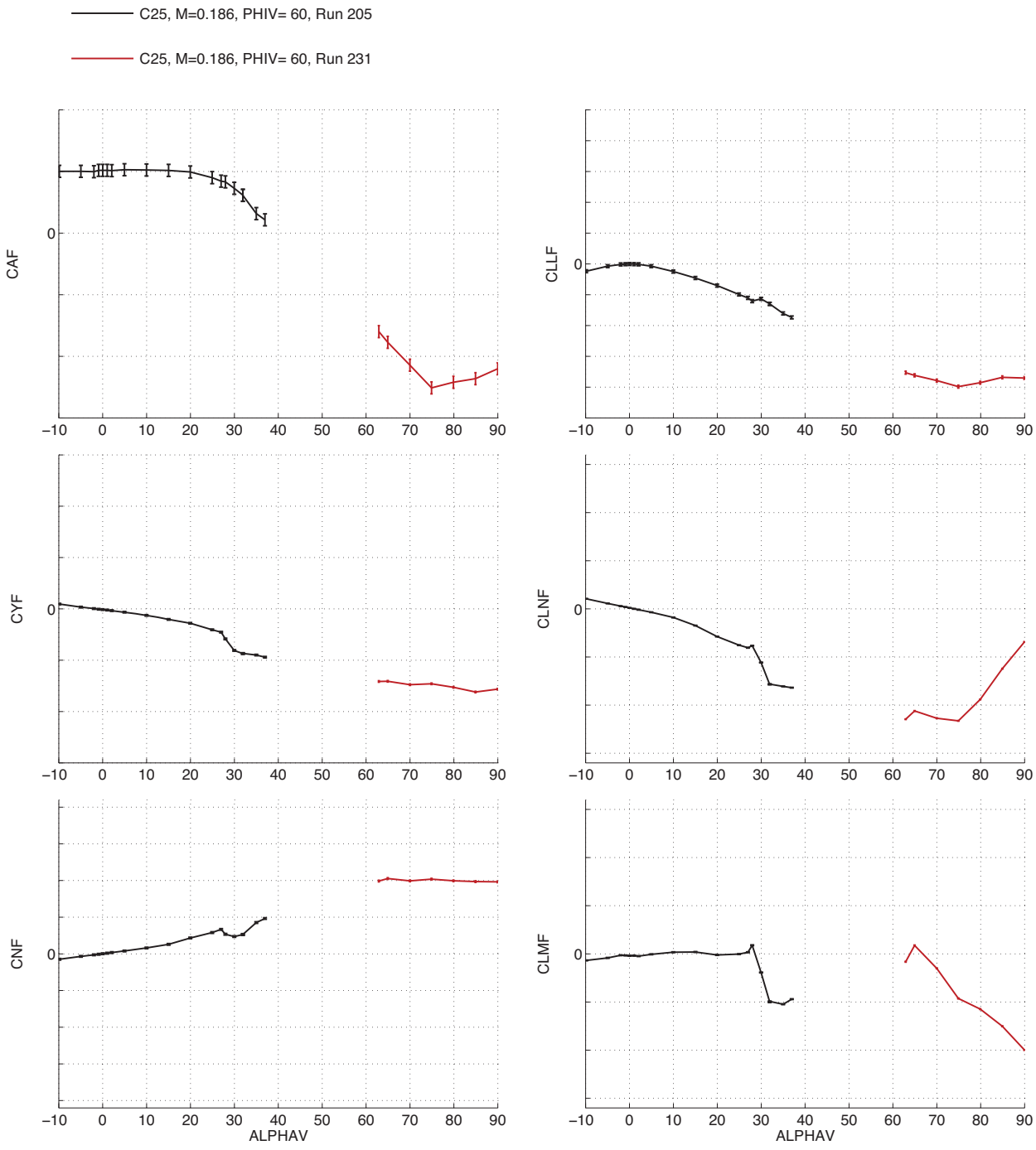

Figure 26. Aerodynamic coefficients for SLS-28000, pitch sweeps at $\phi_V = 60°$.

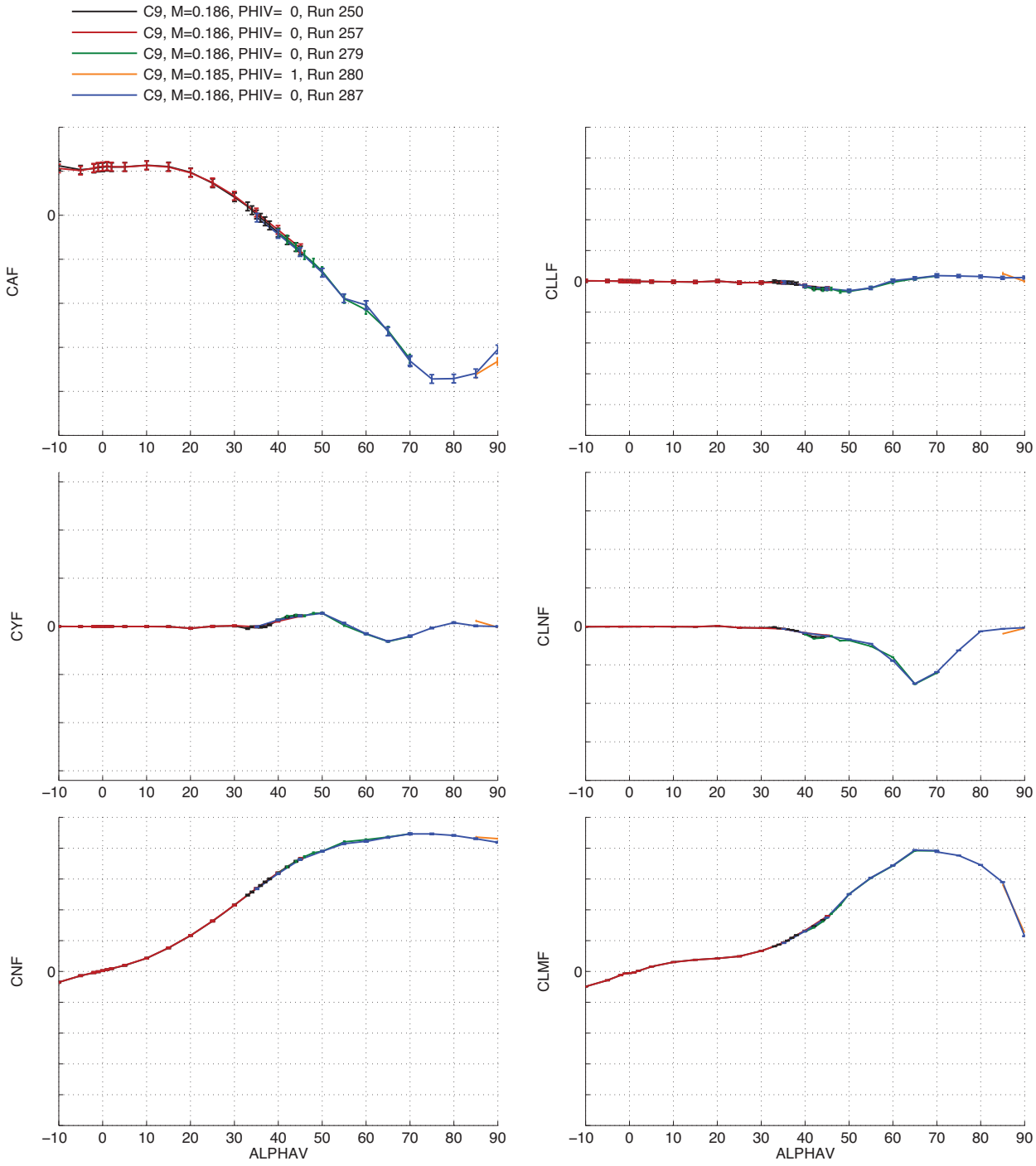

Figure 27. Aerodynamic coefficients for SLS-21000, pitch sweeps at $\phi_V = 0°$.

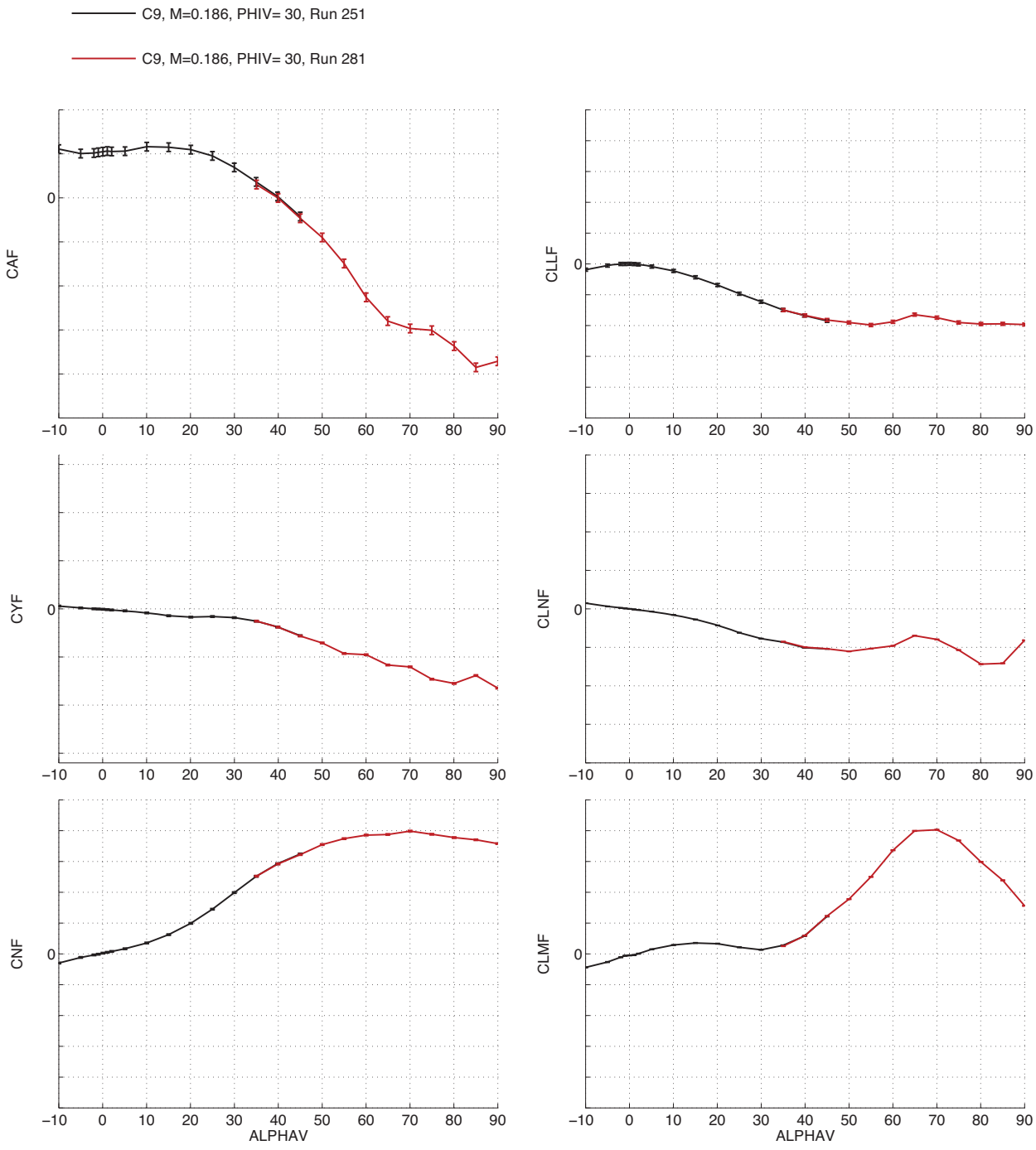

Figure 28. Aerodynamic coefficients for SLS-21000, pitch sweeps at $\phi_V = 30°$.

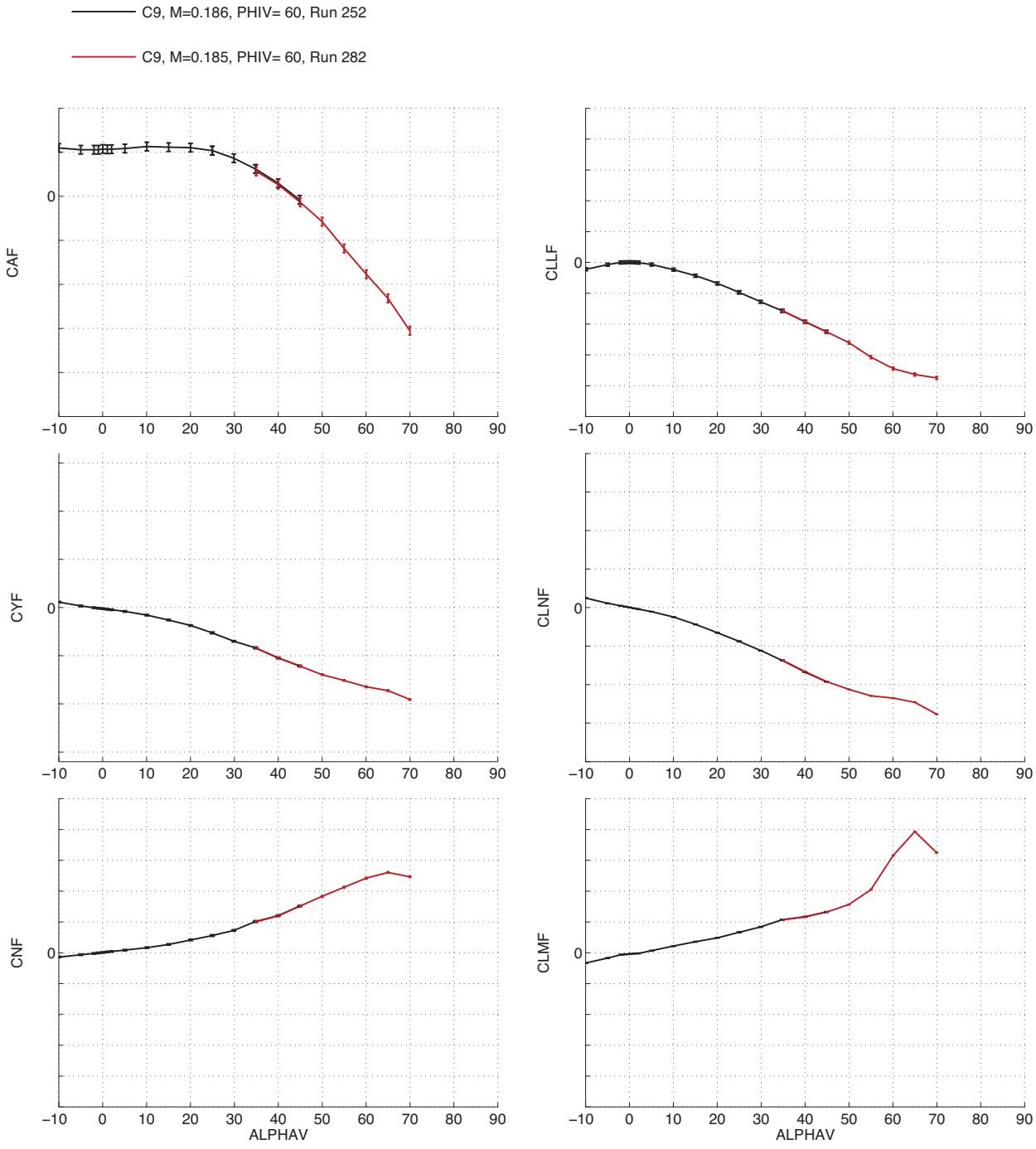

Figure 29. Aerodynamic coefficients for SLS-21000, pitch sweeps at $\phi_V = 60°$.

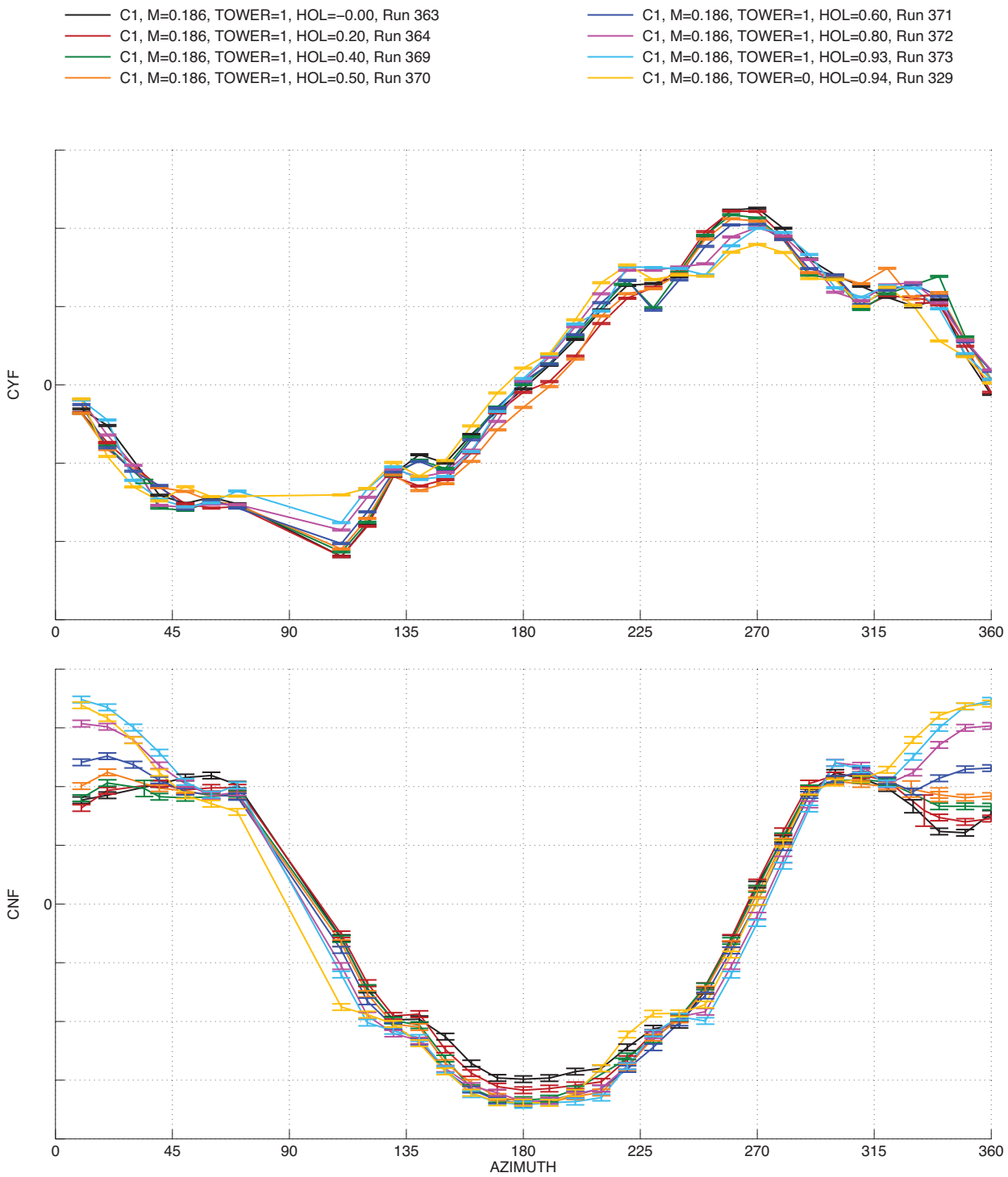

Figure 30. Aerodynamic coefficients for SLS-10000, azimuth sweeps with tower effects, at various heights above the launch pad.

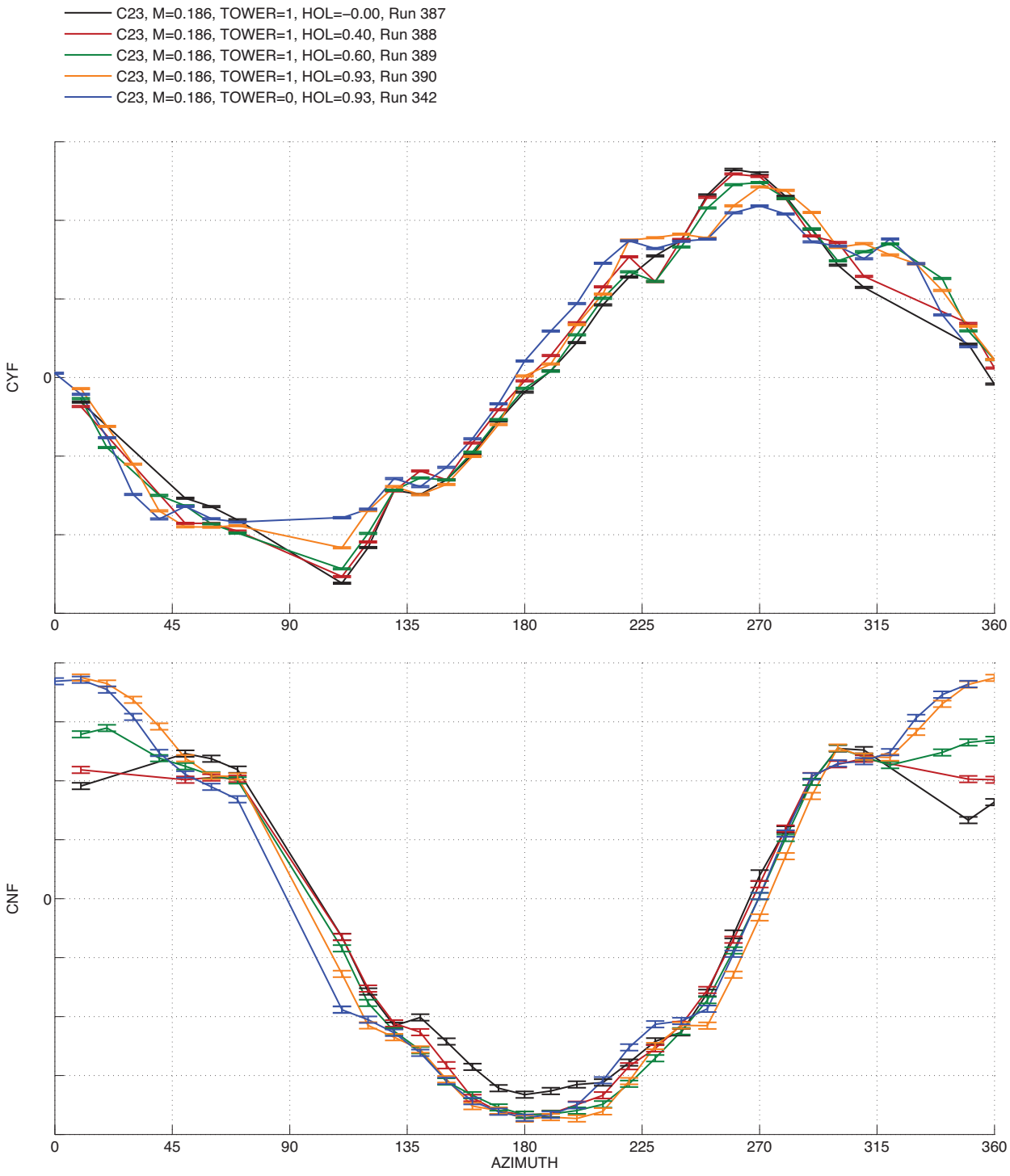

Figure 31. Aerodynamic coefficients for SLS-27000, azimuth sweeps with tower effects, at various heights above the launch pad.

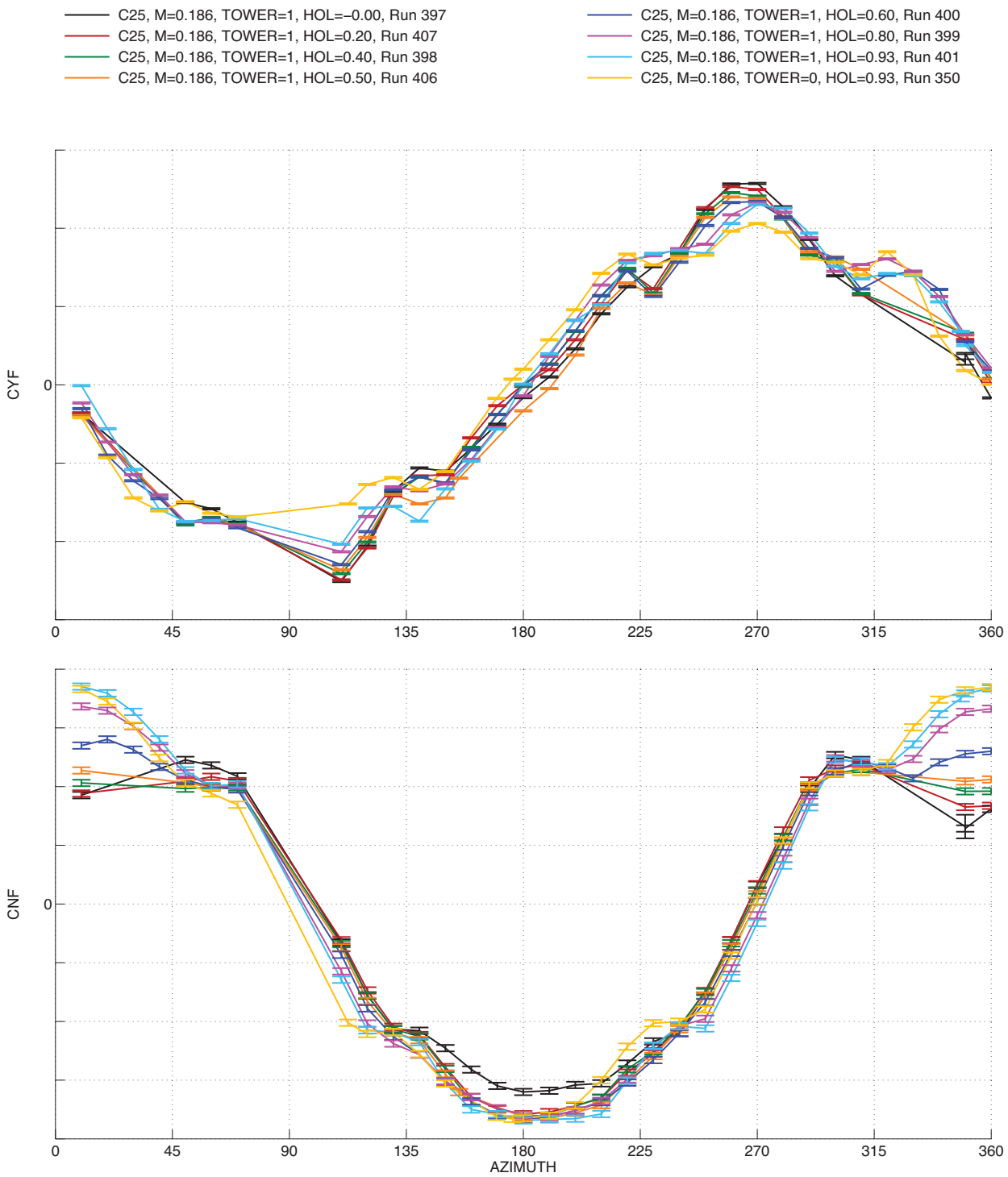

Figure 32. Aerodynamic coefficients for SLS-28000, azimuth sweeps with tower effects, at various heights above the launch pad.

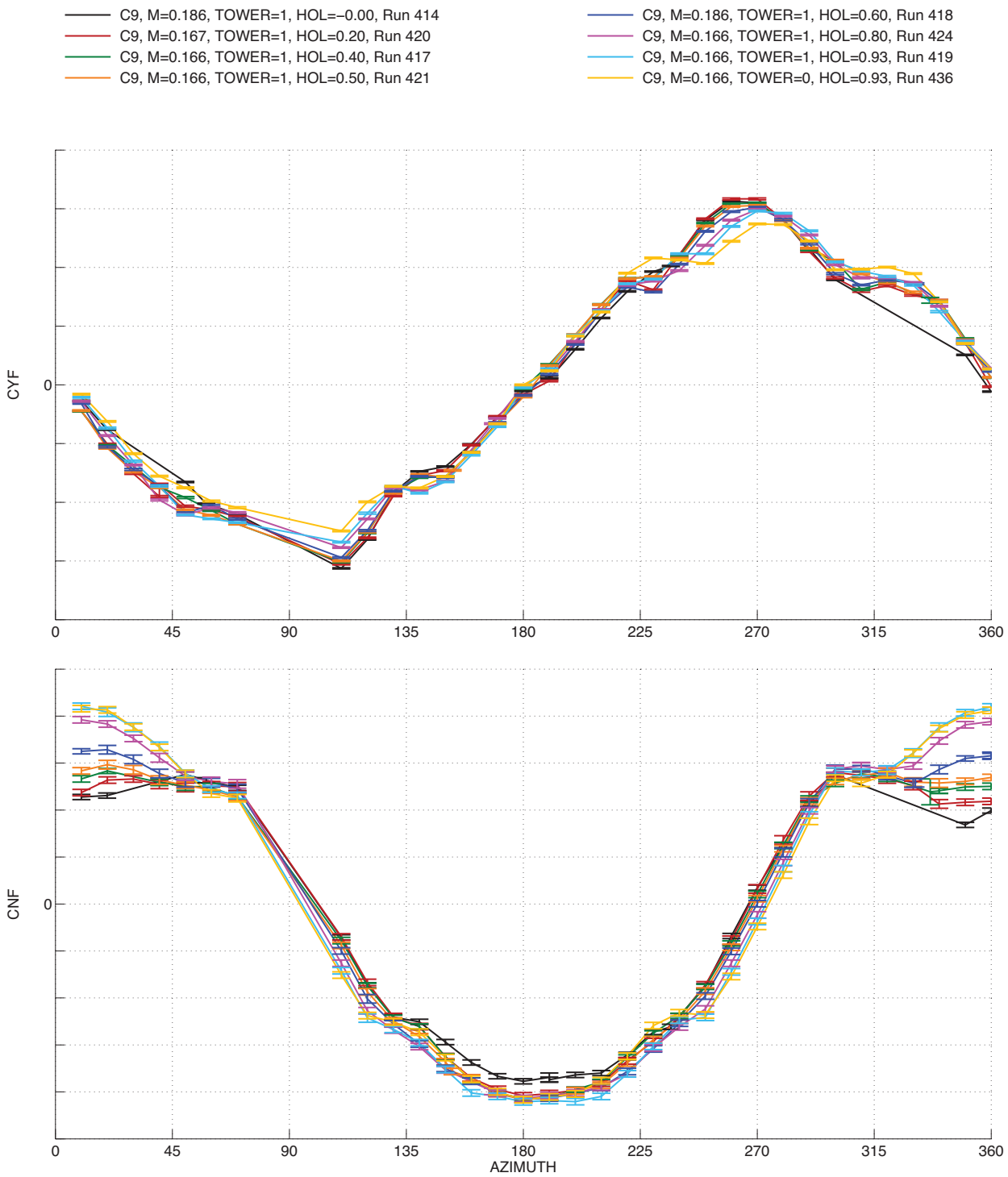

Figure 33. Aerodynamic coefficients for SLS-21000, azimuth sweeps with tower effects, at various heights above the launch pad.